European Journal of Mechanics B/Fluids 21 (2002) 185–206

Solitary waves and conjugate flows in a three-layer fluid

Per-Olav Rusås [1], John Grue *

Department of Mathematics, University of Oslo, Box 1053 Blindern, NO-0316 Oslo, Norway

Received 11 April 2001; received in revised form 16 August 2001; accepted 17 August 2001

Abstract

Interfacial symmetric solitary waves propagating horizontally in a three-layer fluid with constant density of each layer are investigated. A fully nonlinear numerical scheme based on integral equations is presented. The method allows for steep and overhanging waves. Equations for three-layer conjugate flows and integral properties like mass, momentum and kinetic energy are derived in parallel. In three-layer fluids the wave amplitude becomes larger than in corresponding two-layer fluids where the thickness of a pycnocline is neglected, while the opposite is true for the propagation velocity. Waves of limiting form are particularly investigated. Extreme overhanging solitary waves of elevation are found in three-layer fluids with large density differences and a thick upper layer. Surprisingly we find that the limiting waves of depression are always broad and flat, satisfying the conjugate flow equations. Mode-two waves, obtained with a periodic version of the numerical method, are accompanied by a train of small mode-one waves. Large amplitude mode-two waves, obtained with the full method, are close to one of the conjugate flow solutions. © 2002 Éditions scientifiques et médicales Elsevier SAS. All rights reserved.

Keywords: Solitary waves; Three-layer fluids; Overhanging waves

1. Introduction

Internal waves in the ocean are a topic which receive a considerable attention for several reasons. This includes the understanding of fundamental aspects like the wave propagation itself. Furthermore, internal waves may induce loads on floating marine structures, or on members of such structures, and on connected equipment such as cables or risers. It is of importance to predict the wave induced loads and motions of the structures and the connected equipment (see, e.g., Grue et al. [1], Section 1). Other important topics in relation to internal waves are many. Examples are included in, e.g., Duda and Farmer [2], where a state-of-the art of the field may also be found.

Internal waves may attain a relatively large amplitude due to the generally small density variation in the ocean. This suggests that fully nonlinear models of the waves are required. Existing fully nonlinear models mainly fall into two categories. The first includes propagation of internal waves along a continuous stratification (Tung et al. [3]; Turkington et al. [4]; Lamb [5]; Grue et al. [6]). In the second category, interfacial waves may propagate in a two-layer fluid (Amick and Turner [7]; Pullin and Grimshaw [8]; Turner and Vanden-Broeck [9,10]; Grue et al. [1,11]). In the latter case, however, the effect of a finite thickness of the pycnocline is neglected.

The efficiency of two-layer interfacial wave models may be extended to also account for a third fluid layer, or even several layers. This is relevant to conditions in the ocean, see, e.g., Phillips [12] (his Figs. 6.9–11). In a two-layer fluid with constant density in each of the layers, waves of mode-one may propagate. Generally waves of mode number up to $n-1$ may propagate in a fluid with n constant density layers. Thus, another motivation for generalizing a two-layer model to several layers is precisely the possibility to investigate solitary waves of higher modes than one.

---

* Correspondence and reprints.

E-mail addresses: per.o.rusas@hiof.no (P.-O. Rusås), johng@math.uio.no (J. Grue).

[1] Present address: Østfold College, Faculty of Computer Sciences, Box 1192, No-1705 Sarpsborg, Norway.

PII: S0997-7546(01)01163-3

We develop here a fully nonlinear three-layer model. An upper and a lower layer, with constant density in each layer, are separated by a third layer with a density that is assumed to be constant. We investigate internal solitary waves of mode-one or mode-two which are stationary in a frame of reference following the waves. (Mode-one and mode-two waves correspond to the fast and slow linear propagation speeds obtained from the dispersion relation for three-layer fluid discussed in Section 3.2). The model is applicable to steep and even overhanging waves. The mathematical problem is formulated in terms of complex analysis. Discontinuous tangential velocities and continuity of pressure are imposed at the boundary between the layers.

We develop in parallel the equations governing conjugate flows comparing with the general three-layer model. Conjugate flows in a two-layer fluid were studied by Benjamin [13], Mehrotra and Kelly [14], Amick and Turner [7], Turner and Vanden-Broeck [10], Kakutani and Yamasaki [15]. In parallel to our work, Lamb [16] investigated conjugate flows for a three-layer fluid, arriving at the same equations as ours.

The models are applied to investigate extreme waves. Existing results for limiting (overhanging) waves of elevation in two-layer fluid (Pullin and Grimshaw [8]) are generalized to three-layer fluid. In contrast to the limiting waves of elevation, however, all computations of waves of depression with very large amplitude showed non-overhanging profiles. This means that the limiting form of waves of depression are broad and flat, according to the present computations. This is different from what was indicated by the computations of Pullin and Grimshaw [8].

Mode-two waves, obtained with a periodic version of the numerical method, are accompanied by a train of small mode-one waves. Mode-two waves have previously been investigated by Davis and Acrivos [17], Tung et al. [3], Akylas and Grimshaw [18], Michallet and Dias [19,20]. The fact that a train of lower-mode short waves may ride on solitary waves of higher mode than one is also noted for equatorial Rossby waves, see Boyd [21].

The paper is organized as follows: following the introduction, Section 2 describes the mathematical formulation, the nonlinear integral method and the solution procedure. The equations of the conjugate flows are outlined in Section 3. This section includes results for waves of mode-one and mode-two. Extreme waves are investigated in Section 4. Section 5 contains a conclusion.

2. Nonlinear boundary integral model

The density within each layer is constant. The layers will in the following be named by numbers 1, 2 and 3, as shown in Fig. 1. These numbers will be used as indexes for the physical parameters, referring to which layer they belong. In each layer we assume irrotational motion of an incompressible, homogeneous and inviscid fluid. As done by Grue et al. [11], a frame of reference moving with the wave is chosen. We introduce a coordinate system O-xy with the x-axis at the level of the lowest interface, I, in the far-field, and the y-axis pointing upwards, i.e. in the opposite direction of gravity. The upper interface is named J. The domain of fluid k is denoted by Ω_k. The density of the layers is denoted by ρ_k, and the depth of the layers (at rest) is h_k, where $k = 1, 2, 3$. There are rigid walls at $y = -h_1$ and at $y = h_2 + h_3$.

2.1. Mathematical formulation

Complex analysis is applied. We introduce the complex coordinate $z = x + iy$ (see Fig. 1) and the complex velocities $q_k = u_k - iv_k$, $k = 1, 2, 3$, where u_k and v_k denote horizontal and vertical velocity, respectively. For irrotational flow of ideal fluid within each layer, the complex velocity is an analytic function of z. Applying Cauchy's integral theorem, and following

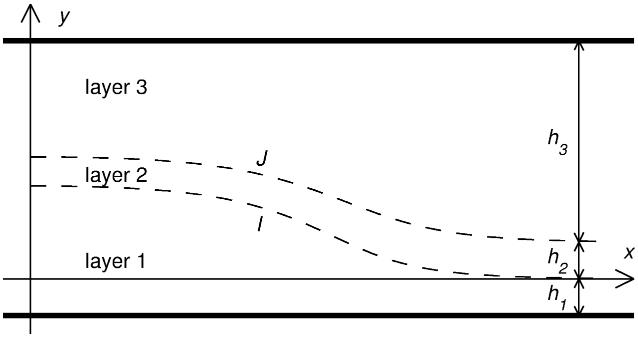

Fig. 1. Sketch of the three-layer fluid. The dashed lines are the interfaces of an actual solution near the Boussinesq limit. Such solutions are thoroughly discussed in Section 3.2. The interfaces are symmetric about $x = 0$, and only the right parts are shown. The vertical direction is stretched by a factor two.

the procedure of Grue et al. [1] and [11], we arrive at the following integral equation involving the complex velocity of the lower layer:

$$\mathrm{PV}\int_I \frac{q_1(z)+c}{z'-z}\,\mathrm{d}z - \int_I \frac{q_1^*(z)+c}{z'-z^*+2\mathrm{i}h_1}\,\mathrm{d}z^* = \begin{cases} 2\pi\mathrm{i}(q_1(z')+c), & z'\in\Omega_1, \\ \pi\mathrm{i}(q_1(z')+c), & z'\in I, \end{cases} \tag{1}$$

where an asterisk denotes complex conjugate and PV principal value. The latter only applies when $z'\in I$. Here we have assumed that $q+c$ rapidly approaches zero when $|x|\to\infty$. Further, we have applied the method of images where the interface I is reflected about the flat bottom at $y=-h_1$. The integration is then along I and its reflection about $y=-h_1$, instead of around the curve enclosing Ω_1. The complex velocity on the reflected interface is equal to the complex conjugate of the velocity q_1 on I. This assures that the rigid lid condition is satisfied at $y=-h_1$.

Applying Cauchy's integral theorem to q_2+c, integrating along a curve enclosing Ω_2, we obtain

$$\mathrm{PV}\int_I \frac{q_2(z)+c}{z'-z}\,\mathrm{d}z - \int_J \frac{q_2(z)+c}{z'-z}\,\mathrm{d}z = \begin{cases} -2\pi\mathrm{i}(q_2(z')+c), & z'\in\Omega_2, \\ -\pi\mathrm{i}(q_2(z')+c), & z'\in I. \end{cases} \tag{2}$$

For $z'\in J$, the expression is similar, except that the integral over J is the principal value integral. The integration along I and J is from $x=-L$ to $x=L$, where $L\to\infty$.

Following the same procedure as for layer 1, we obtain an integral equation involving q_3:

$$\mathrm{PV}\int_J \frac{q_3(z)+c}{z'-z}\,\mathrm{d}z - \int_J \frac{{q_3}^*(z)+c}{z'-z^*-2\mathrm{i}(h_2+h_3)}\,\mathrm{d}z^* = \begin{cases} -2\pi\mathrm{i}(q_3(z')+c), & z'\in\Omega_3, \\ -\pi\mathrm{i}(q_3(z')+c), & z'\in J. \end{cases} \tag{3}$$

As in Eq. (1) the principal values in Eqs. (2) and (3) only apply when z' is on either interface.

Since we have chosen a frame of reference in which the flow is stationary, the kinematic conditions are fulfilled by requiring the velocities at the interfaces to be tangential to I and J. Thus, the complex velocity on, e.g., I in layer 1, say q_{1I}, may be expressed as $q_{1I}=\phi_{1Is}/z_{Is}$. Here ϕ_{1I} is the real velocity potential in layer 1, along interface I, z_I means that z is on I, and $(\,)_s$ means partial derivation with respect to the arc length s along the interface.

The dynamic conditions are easily obtained by applying the Bernoulli equation for the pressure. Continuous pressure at layer I and J then gives

$$\frac{1}{2}\rho_1\bigl(c^2-{\phi_{1Is}}^2\bigr)-\frac{1}{2}\rho_2\bigl(c^2-{\phi_{2Is}}^2\bigr)-(\rho_1-\rho_2)g\,\mathrm{Im}(z_I)=0,\quad z\in I, \tag{4a}$$

$$\frac{1}{2}\rho_2\bigl(c^2-{\phi_{2Js}}^2\bigr)-\frac{1}{2}\rho_3\bigl(c^2-{\phi_{3Js}}^2\bigr)-(\rho_2-\rho_3)g\bigl(\mathrm{Im}(z_J)-h_2\bigr)=0,\quad z\in J. \tag{4b}$$

Here, the values used for the Bernoulli head in each layer are found from the conditions of the flow in the far-field.

Discrete equations and the computational algorithm are given in Appendix A.

2.2. Accuracy

The results presented in the following sections are all tested to converge, and graphical accuracy is achieved. The number of discrete points at the two interfaces are always chosen to be equal, varying from 100 to 240 on each interface, depending on the steepness of the wave. In two examples N is chosen to be 300 and 600.

Since the points are distributed at equal intervals along the interfaces, and not along the horizontal axis, very steep or even overhanging waves are easily calculated and verified to converge.

3. Solitary waves and conjugate flows

The derived equations are then applied to compute waves of permanent form. We perform computations of three-layer and two-layer flows in parallel. A natural starting point is to compare results obtained by the full equations with simplified conjugate flows solutions.

As mentioned in the Introduction, conjugate flows for two-layer fluids are described by Benjamin [13], Mehrotra and Kelly [14], Amick and Turner [7], Turner and Vanden-Broeck [10] and extended to a two-layer fluid with a free surface by Kakutani and Yamasaki [15] (assuming weak nonlinearity). In parallel to our work, Lamb [16] has investigated conjugate flows for a three-layer fluid, arriving at the same equations that are given below.

In the frame of reference moving with the wave speed c the flow is stationary with fluid velocity in the far-field being $-c$. At $x=0$ we denote a_I and a_J as vertical elevations of the interfaces I and J, respectively, relative to the undisturbed lower interface I. Conservation of mass gives

$$-ch_1 = u_1(h_1+a_I), \tag{5a}$$

$$-ch_2 = u_2(a_J-a_I), \tag{5b}$$

$$-ch_3 = u_3(h_2+h_3-a_J), \tag{5c}$$

where u_k, $k=1,2,3$, are the uniform velocities in the respective layers at $x=0$. Continuity of pressure at the interfaces yields

$$\frac{1}{2}\rho_1\bigl(c^2-{u_1}^2\bigr)-\frac{1}{2}\rho_2\bigl(c^2-{u_2}^2\bigr)-(\rho_1-\rho_2)ga_I=0, \tag{6a}$$

$$\frac{1}{2}\rho_2\bigl(c^2-{u_2}^2\bigr)-\frac{1}{2}\rho_3\bigl(c^2-{u_3}^2\bigr)-(\rho_2-\rho_3)g(a_J-h_2)=0. \tag{6b}$$

Conservation of momentum gives

$$\int\limits_{x=\infty}\bigl(p+\rho u^2\bigr)\,\mathrm{d}y=\int\limits_{x=0}\bigl(p+\rho u^2\bigr)\,\mathrm{d}y. \tag{7}$$

By utilizing Bernoulli's equation for the pressure, (7) becomes

$$\begin{aligned}&-\frac{1}{2}\rho_1(a_I+h_1)\bigl(c^2-u_1^2\bigr)+\rho_1a_Ic^2-\frac{1}{2}\rho_2(a_J-a_I)\bigl(c^2-u_2^2\bigr)+\rho_2(a_J-a_I-h_2)c^2\\&\quad-\frac{1}{2}\rho_3(h_2+h_3-a_J)\bigl(c^2-u_3^2\bigr)+\rho_3(h_2-a_J)c^2-\frac{1}{2}g(\rho_1-\rho_2)a_I^2-\frac{1}{2}g(\rho_2-\rho_3)(a_J-h_2)^2=0.\end{aligned} \tag{8}$$

By substituting (5a)–(5c) into (6a), (6b) and (8), a set of equations to determine c, a_I and a_J is obtained. Solution(s) of the equations are obtained by Newton–Raphson's method.

In the Boussinesq limit Eqs. (6a), (6b) and (8) simplify and become, respectively:

$${u_2}^2-{u_1}^2-g'a_I=0, \tag{9a}$$

$${u_3}^2-{u_2}^2-g'(a_J-h_2)=0, \tag{9b}$$

$$\bigl(u_1^2-u_2^2\bigr)a_I+\bigl(u_2^2-u_3^2\bigr)(a_J-h_2)+h_1u_1^2+h_2u_2^2+h_3u_3^2-Hc^2-\frac{1}{2}g'\bigl(a_I^2+(a_J-h_2)^2\bigr)=0, \tag{10}$$

where $g'=g(\rho_1-\rho_3)/\rho_1$, $\rho_2=(\rho_1+\rho_3)/2$ and $H=h_1+h_2+h_3$.

3.1. *Mode-one conjugate flows*

Mode-one conjugate flows are then considered. Three-layer conjugate flows are compared with corresponding two-layer flows. We let the layer thicknesses of the latter, $\hat{h}_1$ and $\hat{h}_3$, be related to the layer thicknesses of the three-layer fluid by

$$\hat{h}_1=h_1+\frac{h_2}{2},\qquad \hat{h}_3=h_3+\frac{h_2}{2}. \tag{11}$$

It follows that $0\leqslant h_2\leqslant 2\hat{h}_1$ for $h_1\geqslant 0$. Further, in the two-layer fluid, the density of the lower layer is ρ_1 while the density of the upper layer is ρ_3.

The solution of two-layer conjugate flows is obtained from our equations by putting $h_2=0$, giving (Amick and Turner [7])

$$\hat{a} = \frac{\sqrt{\rho_1}\hat{h}_3-\sqrt{\rho_3}\hat{h}_1}{\sqrt{\rho_1}+\sqrt{\rho_3}}, \tag{12}$$

$$\hat{c}^2 = \frac{g(\rho_1-\rho_3)(\hat{h}_1+\hat{a})(\hat{h}_3-\hat{a})}{\rho_1(\hat{h}_3-\hat{a})+\rho_3(\hat{h}_1+\hat{a})}, \tag{13}$$

(with our notation) where $\hat{c}$ and $\hat{a}$ denote the propagation speed and amplitude, respectively, of the collapsed interfaces I and J.

Mode-one results of conjugate flows are displayed in Figs. 2(a)–2(c). The density ratios are representative for fresh water and sea water: $\rho_3/\rho_1=0.9775$ and $\rho_2=(\rho_1+\rho_3)/2$, thus quite close to the Boussinesq limit. Results are shown for all possible values of $h_2/\hat{h}_1$ and for a wide range of relative thickness of the upper layer ($2<\hat{h}_3/\hat{h}_1<512$). The differences between the

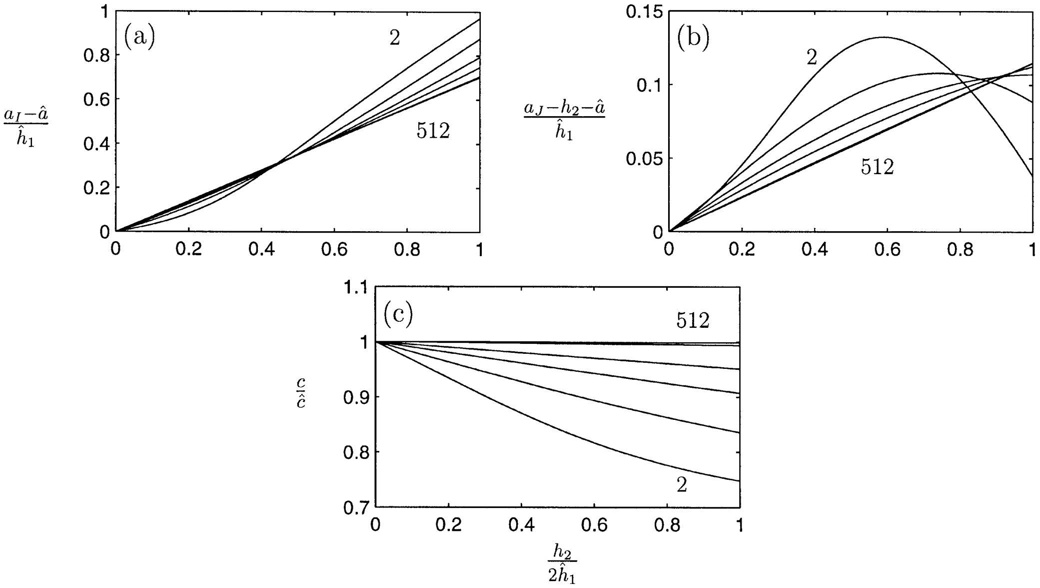

Fig. 2. Comparison of mode-one conjugate flows for three- and two-layer fluids. (a) $(a_I-\hat a)/\hat h_1$; (b) $(a_J-h_2-\hat a)/\hat h_1$) and (c) $c/\hat c$ as function of $h_2/(2\hat h_1)$. Results are shown for $\hat h_3/\hat h_1 = 2, 4, 8, 16, 128, 512$. The curves with $\hat h_3/\hat h_1$ equal 2 and 512 are labeled. The other curves are filling in monotonically between these outer limits. The curves for the two largest values of $\hat h_3/\hat h_1$ are almost coinciding. Densities are $\rho_3 = 0.9775\rho_1$ and $\rho_2 = (\rho_1+\rho_3)/2$. Densities of the lower and upper layer in the two-layer fluid are ρ_1 and ρ_3, respectively.

elevations of the interfaces and the propagation speed, in the three- and two-layer fluids, are visualized. The propagation speed of the three-layer solution is shown relative to the propagation speed of the two-layer solution. At the two extreme values of $h_2/\hat h_1$, the three-layer fluid degenerates to two layers. (With $h_2 = 0$ we obtain the two-layer solution (12)–(13). With $h_2 = 2\hat h_1$, giving $h_1 = 0$, we obtain a two-layer fluid with thickness h_2 and density ρ_2 of the lower layer.)

We observe from Fig. 2(a) that $(a_I-\hat a)/\hat h_1$ is positive for all calculated combinations of layer thicknesses. This means that the elevation of the lower interface I relative to its undisturbed level is always larger than the elevation of the single interface of the two-layer fluid. The amplitude of the upper interface, $a_J - h_2$, is also larger than the amplitude of the two-layer interface, but the difference between them is smaller. In the two-layer fluid the streamline with maximal elevation is the interface itself. In the three-layer fluid, the streamline of maximal deflection from its undisturbed level is the one coinciding with the lower interface. Thus, the maximal vertical transport distance of a fluid particle in the three-layer flow is larger, and will happen for a fluid particle relatively lower in the flow, than for a two-layer fluid.

The maximum level of the streamline originating from the center position of the middle layer in the far-field, is a relevant measure of the wave amplitude. For later reference G denotes this streamline. It follows from mass conservation that for the flow at $x = 0$, the elevation of G is the mean of the elevation of I and J. Figures 2(a)–2(b) show that the elevation of both I and J are larger than the elevation of the interface of the two-layer fluid. Thus the elevation of G is also larger.

While the maximal amplitude of the three-layer solution is increased compared to the two-layer solution, the propagation speed is lowered (Fig. 2(c)). The relative difference is largest for rather small thicknesses of the upper layer. If, on the other hand, the upper layer has a large thickness, the three-layer propagation speed becomes close to the two-layer solution.

It is noted that c and $\hat c$ become equal and that the normalized differences $a_I - \hat a$ and $a_I - h_2 - \hat a$ become linear functions of $h_2/(2\hat h_1)$ when the relative thickness of the upper layer becomes large ($h_1/h_3 \ll 1, h_2/h_3 \ll 1$). In Appendix B it is derived that

$$\frac{a_I-\hat a}{\hat h_1}=\frac{\sqrt{2}}{2}\frac{h_2}{2\hat h_1},\qquad \frac{a_J-h_2-\hat a}{\hat h_1}=\left(\frac{3\sqrt{2}}{2}-2\right)\frac{h_2}{2\hat h_1}, \tag{14}$$

which are valid in the Boussinesq limit when $h_1/h_3 \ll 1$, $h_2/h_3 \ll 1$. In (14), $\hat a = (\hat h_3 - \hat h_1)/2$. The results in (14) confirm the numerical predictions in Fig. 2 with $\rho_3/\rho_1 = 0.9775$. In the limit $h_2 \to 0$, or $h_1 \to 0$, the two-layer results are recovered. The slopes of $a_I - \hat a$ and $a_I - h_2 - \hat a$ at $h_2 = 0$ and $h_1 = 0$ (for any h_1/h_3 and h_2/h_3) may be obtained from Eqs. (34)–(36) in Appendix B.

So far we have considered only cases when ρ_1, ρ_2 and ρ_3 are comparable. It is of interest to investigate wave properties when the densities are varied. In Fig. 3 results for elevations and propagation speed are presented for a wide range of the density

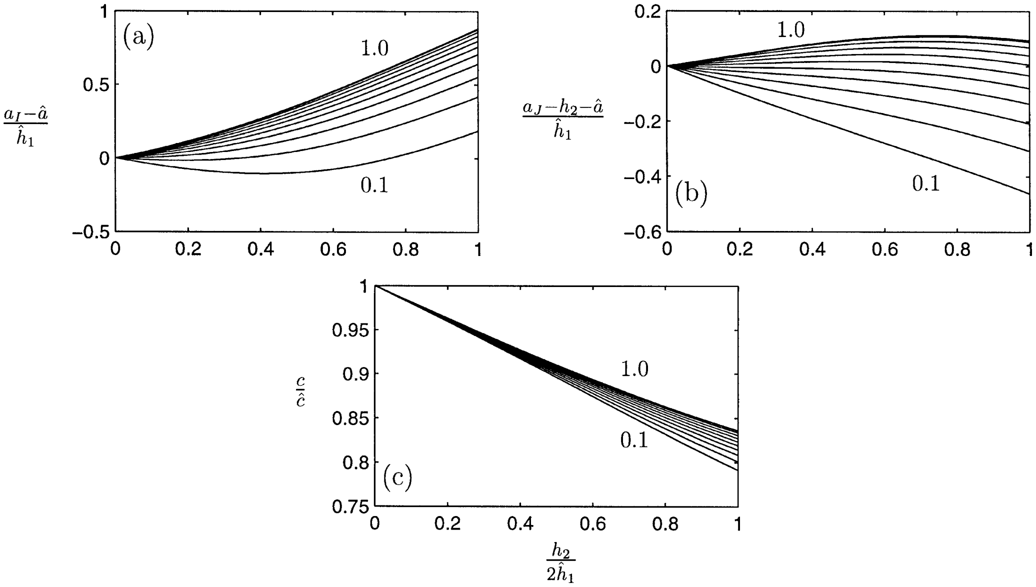

Fig. 3. Comparison of amplitude of interfaces and propagation speed of conjugate flows for three- and two-layer fluid for different densities. (a) $(a_I - \hat{a})/\hat{h}_1$; (b) $(a_J - h_2 - \hat{a})/\hat{h}_1)$ and (c) $c/\hat{c}$ as function of $h_2/(2\hat{h}_1)$. All results with $\hat{h}_3/\hat{h}_1 = 4$. The density differences are the same across the two interfaces. Selected relative densities are $\rho_3/\rho_1 = 0.1, 0.2, 0.3, \ldots, 1.0$ in addition to $\rho_3/\rho_1 = 0.9775$, for which the solutions are graphically coinciding with the results in the Boussinesq limit. The curves for relative densities 0.1 and 1.0 are labeled. The results for the other densities fill in monotonically between these outer limits.

ratio $0.1 \leqslant \rho_3/\rho_1 \leqslant 1$. The density ρ_2 is always $\rho_2 = (\rho_1 + \rho_3)/2$. In the computations a ratio $\hat{h}_3/\hat{h}_1 = 4$ is chosen while the thickness of the middle layer is varied. (There are no difficulties in the computations with $\rho_3/\rho_1 = 1$, since equations with pre-factors proportional to c^2 are normalized by $\hat{c}^2$.)

From Eq. (12) it is evident that the amplitude $\hat{a}$ in two-layer conjugate flows is decreasing with decreasing density ratio ρ_3/ρ_1 (keeping $\hat{h}_3/\hat{h}_1$ fixed). Figure 3(a) shows that a_I and $\hat{a}$ become closer for decreasing ρ_3/ρ_1. This means that a_I is also decreasing with decreasing density-ratio. The elevation of I compared to its undisturbed level is still larger than the elevation of the two-layer interface, however, except for very small ρ_3/ρ_1 and moderate $h_2/(2\hat{h}_1)$ where a_I becomes less than $\hat{a}$.

In the Boussinesq limit the elevation of J in the three-layer fluid is only marginally larger than the elevation of the interface in the two-layer fluid. Figure 3(b) shows that this difference is even smaller when the upper density is decreased. For ρ_3/ρ_1 lower than approximately 0.6 the difference becomes negative.

From Fig. 3(c) we observe that the propagation speed relative to the two-layer propagation speed decreases with decreasing density ratio ρ_3/ρ_1.

3.2. Mode-one results with the complete model

The eigenvalue problem for any number of layers, giving also the dispersion relation, is formulated by Baines [22, Section 4.1]. The dispersion relation for waves in a three-layer fluids was also obtained by Michallet and Dias [20] which in our notation gives for the linear velocity c_0:

$$a_4 c_0^4 - a_2\left(\frac{g}{\nu}\right)c_0^2 + a_0\left(\frac{g}{\nu}\right)^2 = 0, \tag{15}$$

where

$$a_4 = T_3 + RT_1T_2T_3 + S\left(T_1 + \frac{T_2}{R}\right), \tag{16a}$$

$$a_2 = T_1T_3 + T_2T_3 + \frac{T_2S}{R}(T_1 - T_3) - T_1S(T_2 + T_3), \tag{16b}$$

$$a_0 = T_1T_2T_3\left(1 - R + S - \frac{S}{R}\right), \tag{16c}$$

ν is the wavenumber, $T_k = \tanh \nu h_k$ for $k = 1, 2, 3$, $R = \rho_2/\rho_1$ and $S = \rho_3/\rho_1$.

This gives two solutions for c_0^2, a fast mode-one and a slow mode-two wave. With $T_3 = 0$, the two-layer dispersion relation with only a mode-one solution is obtained. In the long wave limit ($\nu h_k \to 0$, $k = 1, 2, 3$) the dispersion relation simplifies to

$$b_4 c_0^4 - g b_2 c_0^2 + g^2 b_0 = 0, \tag{17}$$

where

$$b_4 = h_3 + S\left(h_1 + \frac{h_2}{R}\right), \tag{18a}$$

$$b_2 = h_1 h_3 + h_2 h_3 + \frac{h_2 S}{R}(h_1 - h_3) - h_1 S(h_2 + h_3), \tag{18b}$$

$$b_0 = h_1 h_2 h_3 \left(1 - R + S - \frac{S}{R}\right). \tag{18c}$$

In the Boussinesq limit, with equal density jumps across the interfaces, we obtain

$$c_0^2 = g' \frac{2h_1h_3 + h_1h_2 + h_2h_3 \pm \left[h_2^2(h_1 - h_3)^2 + 4h_1^2h_3^2\right]^{1/2}}{4(h_1 + h_2 + h_3)}, \tag{19}$$

where $g' = g(\rho_1 - \rho_3)/\rho_1$.

We also note that Moni and King [23] studied mode-one solitary waves in a two-layer fluid with a free surface. (They noted that they were unable to find mode-two waves.)

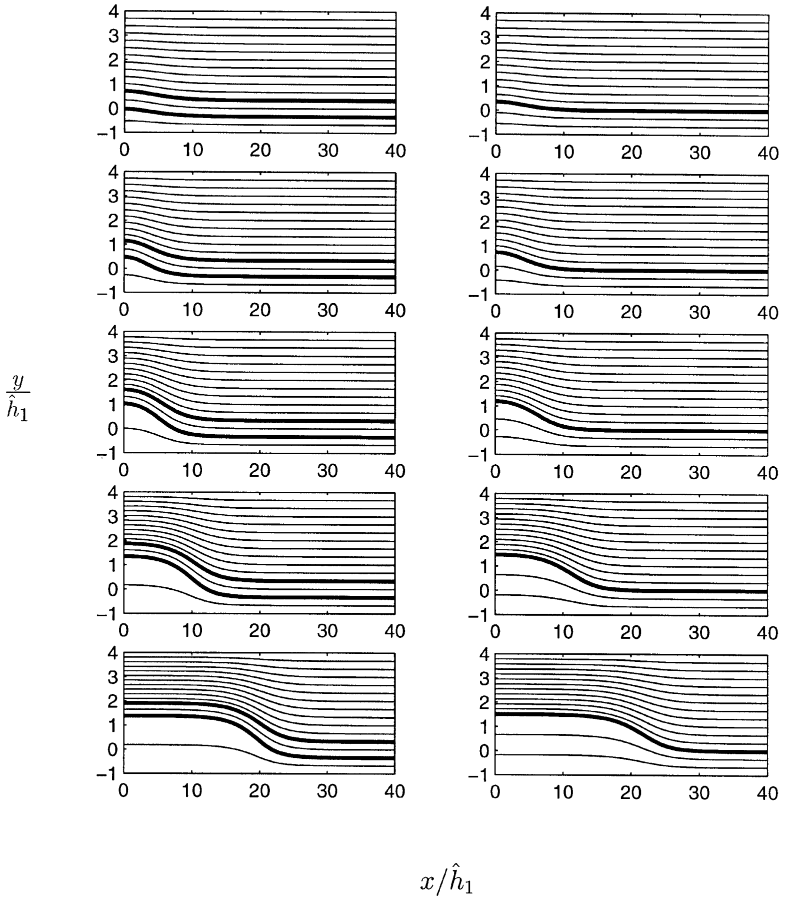

Fig. 4. Streamlines of three-layer solutions (first column) and of two-layer solutions (second column). Only the right halves of the symmetric flows are shown. Note that for the three-layer fluid, the vertical coordinate, y, is shifted $h_2/2$ downwards, such that the undisturbed middle streamline, G, is at $y = 0$. Layer thicknesses are $\hat{h}_3/\hat{h}_1 = 4$ and $h_1 = h_2$. The net volume of the waves are $2, 4, 8, 16, 32\hat{h}_1^2$ under I for the two-layer fluid and under G for the three-layer fluid.

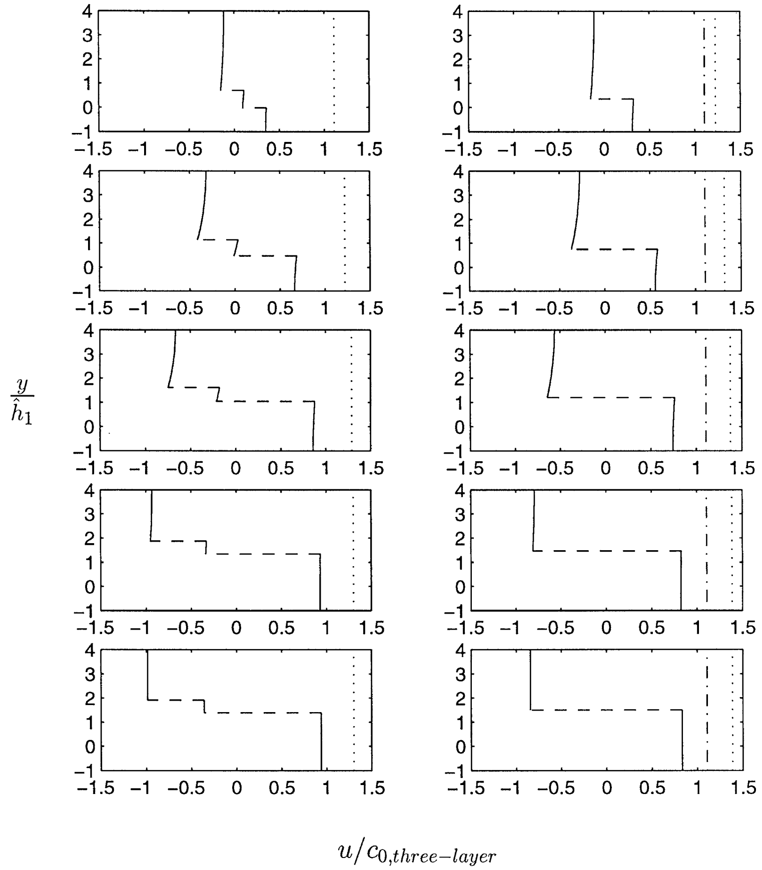

Fig. 5. Velocity profiles of three-layer solutions (first column) and of two-layer solutions (second column) calculated from the solutions in Fig. 4. The vertical dotted lines indicate the value of the propagation speed, and the dash-dot line the linear propagation velocity of the two-layer fluid. All velocities are scaled with the long wave propagation speed of the three-layer fluid, which for these densities and depth ratios is $c_{0,\text{three-layer}} = 0.121\ldots(gh_2)^{1/2}$. The vertical coordinate y for the three-layer solutions is shifted as in Fig. 4. $\hat{h}_3/\hat{h}_1 = 4$, $h_1 = h_2$.

We now exploit the numerical model described in Section 2 to compute moderately steep waves. Further, we obtain information about the region connecting the conjugate flows at $x = 0$ and $x \to \infty$ when the amplitudes are maximal. Focus is directed to a single configuration, with $\hat{h}_3/\hat{h}_1 = 4$ and equal thicknesses of the middle and lower layers, i.e. $h_2 = h_1$. The densities are $\rho_3 = 0.9775\rho_1$ and $\rho_2 = (\rho_1 + \rho_3)/2$. The results in Fig. 2 give elevations $a_I/\hat{h}_1 = 1.73\ldots$ and $a_J/\hat{h}_1 = 2.25\ldots$ and propagation speed $c/c_0 = 1.30\ldots$, where $c_0 = 0.121\ldots(g\hat{h}_1)^{1/2}$ is the long wave propagation speed of mode-one waves. By calculating a series of solutions with increasing wave elevation we eventually reach a broad and flat solitary wave which has the same values of a_I, a_J and c/c_0 as obtained by the equations of conjugate flow.

Figures 4 and 5 show the streamlines and velocity profiles for some of these solutions. Note that in these figures the streamlines and velocity profiles are shifted an amount $h_2/2 = \hat{h}_1/3$ upwards, such that the undisturbed end of G is at $y = 0$. Similarities with and differences from the corresponding two-layer solutions then become more apparent. Figures 4 and 5 clearly confirm that the elevation of the interfaces of the three-layer conjugate flow, compared to their undisturbed level, is larger than for the conjugate flows in the two-layer fluid. (In Figs. 4 and 5 the net volume of the wave, below G of the three-layer solution and below I of the two-layer solution, is $2, 4, 8, 16, 32\hat{h}_1^2$.)

We observe in Fig. 5 that although the propagation speed is smaller for the three-layer solution, the fluid velocity is larger in the lower and upper layers. (The horizontal velocity of the two-layer fluid is in the figure scaled by the long wave propagation speed $c_0 = 0.121\ldots(g\hat{h}_1)^{1/2}$ of the three-layer fluid.)

Figure 6 visualizes the elevations of I, J and G as functions of the propagation speed, and compares with the two-layer solution. The propagation speed is again smaller for the three-layer fluid. The increased elevation of the streamline G for conjugate flows, compared to the elevation of the two-layer interface, is small but noticeable.

The discussed three-layer results give evidence of the existence of three-layer mode-one conjugate flows as part of broad stationary solutions. We have also performed several additional numerical calculations (not reported here) with the same density

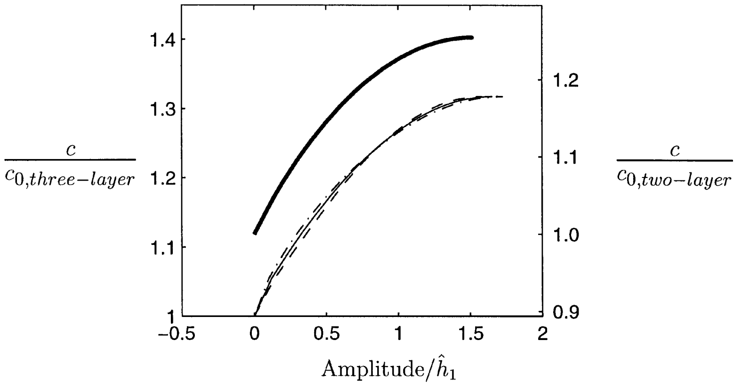

Fig. 6. Propagation speed as function of amplitude of I (dash-dot line), J (thin solid line) and G (dashed line) for the three-layer solutions, and as function of the amplitude of the single interface (thick solid line) for the two-layer solution. The propagation speeds are scaled by the linear long wave speed of the three-layer fluid (left vertical axis) and the two-layer fluid (right vertical axis).

differences close to the Boussinesq limit and with $\hat{h}_3/\hat{h}_1$ up to 50. For all layer thicknesses considered we found broad and flat-crested solutions. In Section 4 we investigate similar solutions, except that the density differences between the layers are much larger. With large thicknesses of the upper layer, we do not find broad solutions with properties of conjugate flows. Instead, steep and overhanging solutions are found. Computations with a thick lower layer, i.e. $h_1/h_2 \gg 1$, $h_2 = h_3$ and ρ_3/ρ_1 far from unity, exhibit broad and flat-crested solutions in accordance with conjugate flows, however.

3.3. Integral properties of the mode-one solutions

Various relations for integral properties like mass, momentum and kinetic energy are derived in Appendix C. The values of these properties are used as a check on the computations, see Rusås [24].

3.4. Waves of mode-two

Solitary waves of mode-two [17–21] may have oscillatory short mode-one waves superimposed on the tail traveling with the same speed as the mode-two wave, termed generalized solitary waves. We aim to supplement existing computations of mode-two waves using the present three-layer model. It is tempting to start with the corresponding three-layer model of conjugate flows, as also investigated by Lamb [16].

In the computations of the conjugate flows, the thickness of the outer layers are set equal ($h_1 = h_3$) and we search for solutions for $0 < h_{1,3}/h_2 < 10$. The total number of solutions is found by a graphical method. First c is eliminated using Eq. (8). The two remaining equations are then visualized as curves in a plane with the remaining unknowns, a_I and a_J, on the axes. The solutions are finally found at the crossing points between these curves. The graphical technique was used to identify the number of solutions and to determine initial guesses for Newton–Raphson's method which we use to solve the same equations.

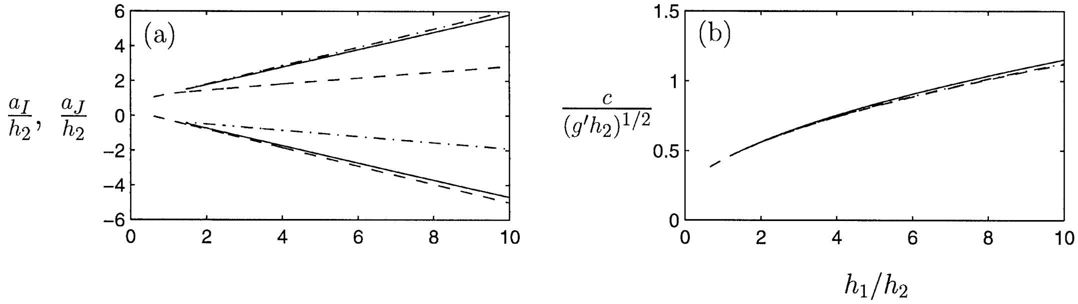

Fig. 7. Scaled amplitudes (a) and propagation speed (b) of three-layer conjugate flows. The thicknesses of the upper and lower layers are equal ($h_1 = h_3$). Densities are $\rho_3 = 0.9775\rho_1$ and $\rho_2 = (\rho_1 + \rho_3)/2$. Three solutions are shown with different linestyles. The propagation speed in (b) is scaled dividing with $(g'h_2)^{1/2}$, where $g' = g(\rho_1 - \rho_3)/\rho_1$ is the reduced gravity.

The same densities as in the previous sections, close to the Boussinesq limit, are chosen. We find that for thicknesses of the lower and upper layer ($h_1 = h_3$) larger than approximately $1.47h_2$ there are three mode-two solutions, while for values of h_1/h_2 less than 1.47 there is only one solution. In addition there is a very small mode-one solution which vanishes in the Boussinesq limit. Figure 7 shows the three mode-two solutions. We observe that there is one nearly symmetric solution about the middle streamline G. The two other solutions are nearly opposite versions of each other. By turning the vertical axis for one solution it nearly coincides with the other. This is expected if we invoke the Boussinesq limit where no preferred vertical direction exists. Thus, if in this limit one solution not symmetric about G exists, the solution turned upside down is also a solution.

The bifurcation described above was also noted by Lamb [16] investigating the Boussinesq limit, finding three solutions for $h_1/h_2 > 1.207\ldots$ (in our notation). Computations using our model with $\rho_3/\rho_1 = 0.9999$ predicts three solutions when $h_1/h_2 > 1.2$, which is in agreement.

In addition to the conjugate flow computations, we have made attempts to calculate mode-two solutions using the full equations derived in Section 2. No satisfactory results were found. Either the iterative scheme broke down or the solutions had mode-one type waves superimposed on the mode-two solution. Such solutions cannot be represented in the numerical scheme, because it is not possible to truncate the apparently infinitely long mode-one type disturbances. The absence of perfectly stationary mode-two solutions of the full method, see also, e.g., Michallet and Dias [19], has motivated us to search for periodic mode-two waves. Then there is no technical truncation problem, and perfectly stationary mode-two solutions with mode-one waves superimposed may exist.

Periodic versions of integral equations (1)–(3) were formulated, utilizing the partial fractions expansion of the cotangent-function. The kinematic and dynamic conditions were left unchanged. A similar periodization was used by Turner and Vanden-Broeck [9] in their investigation of overhanging periodic deep water interfacial waves in a two-layer fluid with infinite layer thicknesses.

An important difference between the non-periodic and periodic formulations is that in the former the flow velocity in the far-field is known to be c along the negative x-axis. This is not generally the case for a periodic solution. Except for layers of infinite thickness, there is no far-field where the velocity is given. Thus an additional condition for each layer is needed to close the set of equations. In the case of non-periodic waves, the flux through any cross section of layer k equals $-h_k c$. We pose this requirement on the periodic waves. Other choices are also possible and some are discussed by Rusås [24] which also gives the details on how the flux requirement is imposed.

Figure 8 shows a series of periodic solutions with $h_1 = h_3 = 4h_2$ and $\rho_3/\rho_1 = 0.9775$, $\rho_2 = (\rho_1 + \rho_3)/2$. The chosen wavelength is $100h_2$. Only one half wavelength of the symmetric wave is shown. The series of computations is initialized by a mode-one wave of moderate amplitude reflected in the line $y = h_2/2$. This yields a symmetric initial guess, which leads to convergence of the iterative method against mode-two waves. Other non-symmetrical initial guesses give mode-one solutions (not shown here).

The waves of increasing amplitude are computed by gradually expanding the volume of the middle layer. The added volume of the layer enters into the dominant mode-two wave. On this wave a train of mode-one waves becomes superimposed. The amplitude of the latter, gradually increasing with the volume of the main wave, is vanishingly small in Fig. 8(a) but has become prominent in Figs. 8(d) and 8(e).

The mode-two wave presented in Fig. 8(d) has depression $\mathrm{Im}(\chi(1)) = -1.7h_2$ of the lower interface and elevation $\mathrm{Im}(\zeta(1)) - h_2 = 0.788\ldots h_2$ of the upper. The scaled propagation velocity is $c/c_0 = 1.53\ldots$. The corresponding quantities in Fig. 8(e) are: $\mathrm{Im}(\chi(1)) = -1.84\ldots h_2$ of the lower interface, $\mathrm{Im}(\zeta(1)) - h_2 = -0.0618\ldots h_2$ of the upper interface and scaled propagation velocity $c/c_0 = 1.54\ldots$.

These values may be compared with the three solutions of conjugate flows (Fig. 7), i.e.,

$$\frac{a_I}{h_2} = \{-1.72\ldots, -1.83\ldots, -0.847\ldots\}, \tag{20}$$

$$\frac{a_J - h_2}{h_2} = \{1.77\ldots, 0.813\ldots, 1.85\ldots\}, \tag{21}$$

$$\frac{c}{c_0} = \{1.59\ldots, 1.56\ldots, 1.57\ldots\}, \tag{22}$$

where $c_0/(gh_2)^{1/2} = 0.0711\ldots$.

While the first of the three solutions in (20)–(22) is approximately symmetric about the middle line of the flow, the second and third solutions are nearly opposite versions of each other, as previously noted. It is evident that the mode-two wave in Fig. 8(d) has values of $\mathrm{Im}(\chi(1))$, $\mathrm{Im}(\zeta(1)) - h_2$ and c/c_0 that are fairly close to the second solution in (20)–(22). A perfect agreement is not expected due to the presence of the mode-one waves, however. The results in Fig. 8(e) has the largest volume we were able to pose in the series of computations. It is observed that the dominant mode-two wave is significantly affected by the mode-one waves in this case. The values of $\mathrm{Im}(\chi(1))$ and $\mathrm{Im}(\zeta(1)) - h_2$ are far from any of the solutions in (20)–(22),

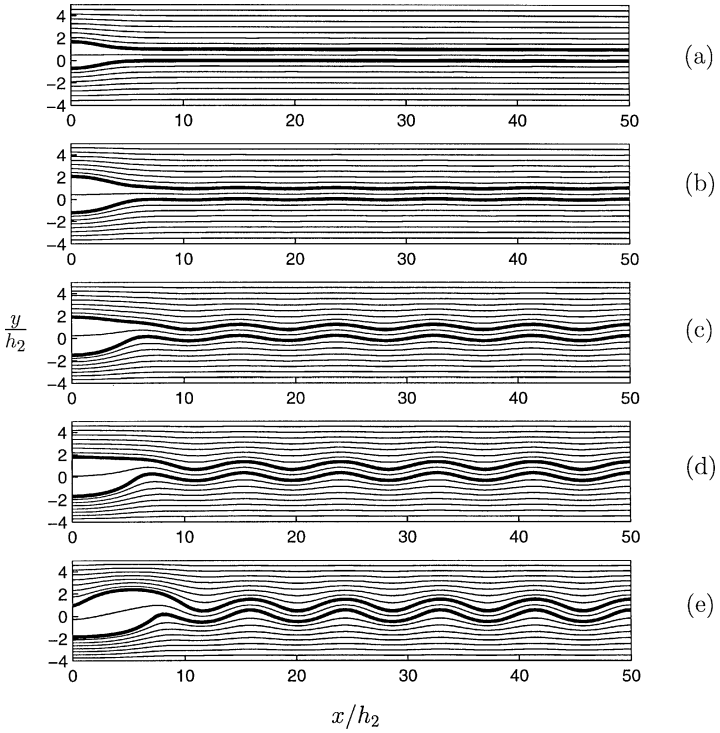

Fig. 8. Streamlines of mode-two periodic three-layer solutions. One half period is shown. Layer thicknesses are $h_1 = h_3 = 4h_2$. Densities are $\rho_3 = 0.9775\rho_1$ and $\rho_2 = (\rho_1 + \rho_3)/2$. The results (a) to (e) are selected from a series of solutions with increasing volume of the middle layer.

however. The waves in Figs. 8(a)–8(e) do of course not approach broad and flat solutions of conjugate flows, as did the mode-one solutions in Section 3.2.

4. Extreme waves

It is of interest to investigate large-amplitude mode-one solitary waves when $\hat{h}_3/\hat{h}_1$ either is much larger or much smaller than unity, and the density ratio ρ_3/ρ_1 is not close to unity.

For interfacial solitary waves Pullin and Grimshaw [8] obtained the following results, which also seem to be the most up-to-date. They considered a two-fluid system where one of the layers had finite thickness while the other was infinitely thick. A rather large range of density ratios was investigated. The main part of their results for interfacial waves concerned solitary waves of elevation with the upper layer being infinitely thick. In this case they found that a large wave always developed a vertical tangent and became overhanging. The wave developed a bubble-capped limiting wave with finite amplitude, termed extreme wave. This result is true for a density ratio not close to unity. In the Boussinesq limit they found no limit of the wave amplitude, however. For waves of depression, in the case of an infinitely thick lower layer, Pullin and Grimshaw gave few results. Their Fig. 11 plots the wave speed as function of the wave amplitude, indicating, however, that a maximal amplitude (and thereby a turning point) occurs for their α equal to 0.2. (This wave on an infinitely thick lower layer, is not broad and flat.) The value $\alpha = 0.2$ corresponds to $\rho_3/\rho_1 = 2/3$ in our notation. Their discussion indicates that the depression wave becomes overhanging, with a turning point in the speed amplitude plot, when the amplitude normalized by the thinner layer thickness is about 8. They indicated, however, that the computations with large amplitude were somewhat uncertain. (They used $N = 40$ discretization points in the computations.)

Prior to Pullin and Grimshaw's work, Meiron and Saffman [25] and Turner and Vanden-Broeck [9] found that periodic waves on the interface between two infinitely thick layers had an overhanging extreme form. They found that this result was true for any (stable) density-ratio, also in the Boussinesq limit.

Motivated by these findings, we investigated extreme waves propagating in the three-layer fluid. Results for two-layer fluid are computed for comparison.

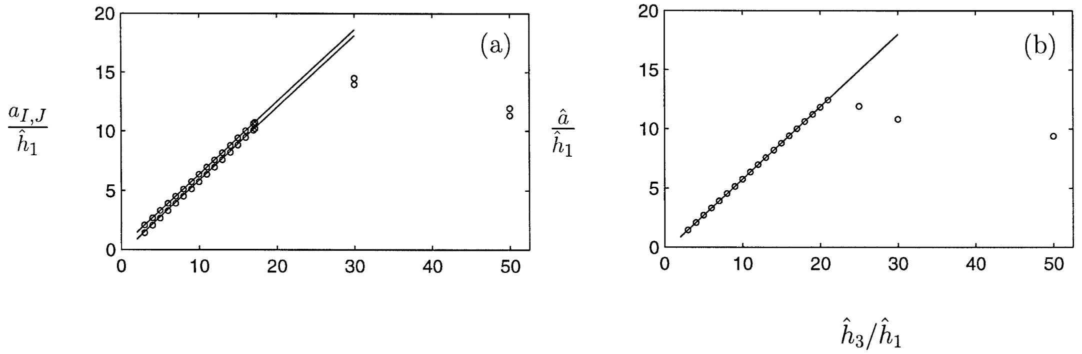

Fig. 9. Maximal amplitudes of the interfaces (a) for the three-layer and (b) for the two-layer fluids as function of upper layer thickness. The solid lines are the results of conjugate flow solutions. The circles are results of the complete model. Densities are $\rho_3/\rho_1 = 0.9775$ and $\rho_2 = (\rho_1 + \rho_3)/2$.

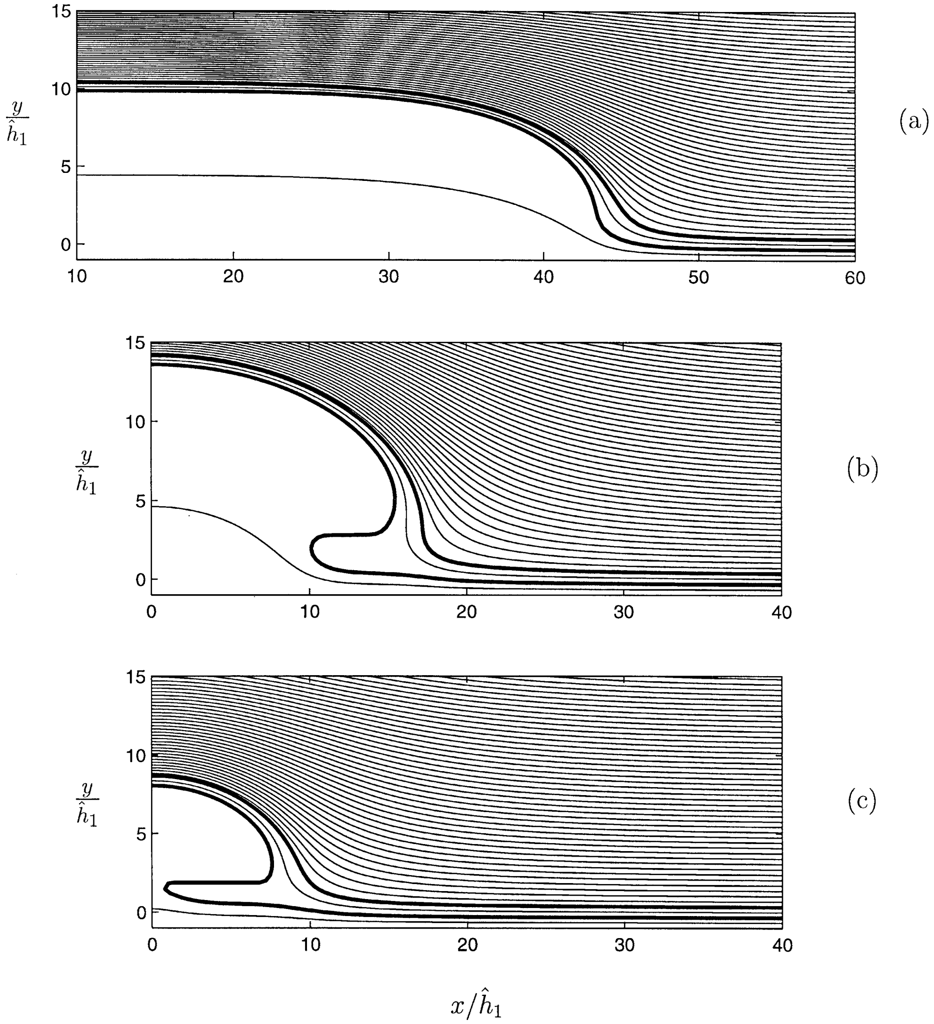

Fig. 10. Extreme three-layer solutions. Relative densities are $\rho_2/\rho_1 = 0.7$ and $\rho_3/\rho_1 = 0.4$. The thicknesses of the lower and middle layers are equal. (a) The highest amplitude broad solution found. Upper layer thickness is $\hat{h}_3 = 17.2\hat{h}_1$. (b) The maximal amplitude solution with upper layer thickness $\hat{h}_3 = 30\hat{h}_1$ and (c) the most overhanging solution found for $\hat{h}_3 = 30\hat{h}_1$. Nonlinear wave velocities in (a)–(c) are, respectively: $c/c_0 = 2.6303\ldots, 3.3109\ldots, 2.7672\ldots$. Linear wave velocities in (a)–(c) are, respectively: $c_0/(g\hat{h}_1)^{1/2} = 0.7534\ldots, 0.7593\ldots, 0.7593\ldots$.

While the computations in Section 3.2 were all close to the Boussinesq limit, we now choose large density ratios: $\rho_3/\rho_1 = 0.4$, $\rho_2/\rho_1 = 0.7$. The value $\rho_3/\rho_1 = 0.4$ gives $\alpha = -0.428$ in Pullin and Grimshaw's notation. Figures 9(a) and 9(b) show the resulting maximal elevations of the interfaces as function of $\hat{h}_3/\hat{h}_1 \leqslant 50$. In the computations $h_2 = h_1$. The wave solutions are broad and flat up to a certain value of the thickness ratio, with elevations very close to those determined by the conjugate flows model. For the three-layer fluid this means $\hat{h}_3/\hat{h}_1$ up to 17.2 and for the two-layer fluid $\hat{h}_3/\hat{h}_1$ up to 21. Above these values of $\hat{h}_3/\hat{h}_1$ we do not find broad wave solutions.

The streamlines of the highest broad solutions we found in the three- and two-layer fluids are visualized in Figs. 10(a) and 11(a). We note that the interface in the two-layer solution is slightly overhanging. For the three-layer fluid we were not, however, able to obtain a solution that is both broad and overhanging. In other words, the overhanging three-layer solutions we were able to find never became broad.

We note that the iterative nonlinear method did not find broad solutions for larger thickness ratio than indicated above. This was true even when the initial guess was extrapolated from solutions with a slightly smaller thickness of the upper layer.

Overhanging waves were computed using the full model for some selected large values of $\hat{h}_3/\hat{h}_1$ in the regime where conjugate flow solutions cannot be reached. In these computations the wave amplitude was increased stepwise up to a maximal value. These maximal elevations of the interfaces, obtained to graphical accuracy, are indicated in Fig. 9. These elevations are considerably smaller than those predicted by the conjugate flow model.

The streamlines in Fig. 10(b) visualize the solitary wave with maximal amplitude in the three-layer fluid when $\hat{h}_3/\hat{h}_1 = 30$ and $h_2/h_1 = 1$. The corresponding two-layer solution is shown in Fig. 11(b) ($\hat{h}_3/\hat{h}_1 = 30$). In both cases the waves are overhanging. The overhanging wave is most pronounced, and the amplitude is largest, in the three-layer fluid.

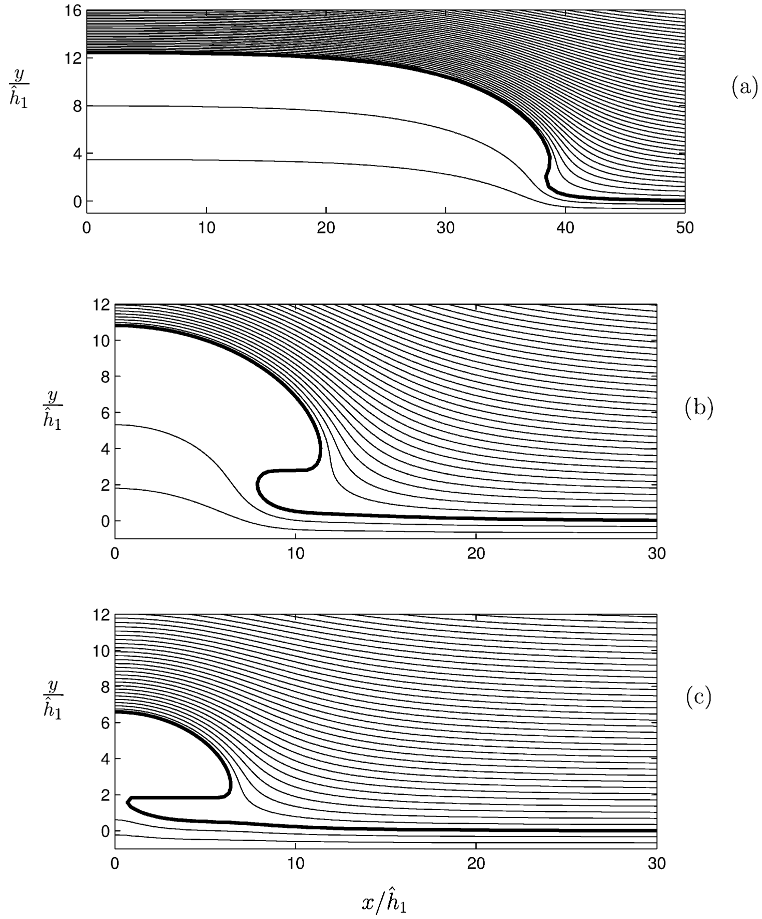

Fig. 11. Extreme two-layer solutions. Densities are $\rho_3/\rho_1 = 0.4$. (a) The highest amplitude broad solution found. Upper layer thickness is $\hat{h}_3 = 21.0\hat{h}_1$. (b) The maximal amplitude solution with upper layer thickness $\hat{h}_3 = 30\hat{h}_1$ and (c) the most overhanging solution found for the same layer thicknesses. Nonlinear wave velocities in (a)–(c) are, respectively: $c/c_0 = 2.2245\ldots, 3.0642\ldots, 2.4977\ldots$. Linear wave velocities in (a)–(c) are, respectively: $c_0/(g\hat{h}_1)^{1/2} = 0.7673\ldots, 0.7695\ldots, 0.7695\ldots$.

After having increased the amplitude stepwise up to its maximum, we pursue the branch of solutions further. The solutions then more and more become overhanging while the amplitude is decreased. Streamlines for extremely overhanging profiles are visualized in Figs. 10(c) and 11(c). We did not succeed in finding waves being more overhanging. This is most probably due to lack of a proper discretization of the sharp bend close to where the interface nearly intersects its symmetric counterpart. The results do indicate, however, that overhanging solutions exist until the interface intersects itself.

Some properties along the whole branches of solutions, from zero amplitude to maximum overhangig waves, are visualized in Fig. 12. We observe that both the propagation velocity and the net volume of the waves are nearly identical for waves in two- and three-layer fluids, except that the solution branch extends to considerably larger amplitude in the three-layer fluid.

Solutions have also been calculated close to the Boussinesq limit for $1 < \hat{h}_3/\hat{h}_1 \leqslant 50$ and $h_2 = h_1$ (results not shown). The solutions were all broad and flat-crested for the layer thicknesses considered.

We have also computed three-layer waves of depression with $\hat{h}_1/\hat{h}_3 = 50$ and $h_2/h_1 = 1$. The densities were the same as for the results discussed above ($\rho_3/\rho_1 = 0.4$, $\rho_2/\rho_1 = 0.7$). The value of $\rho_3/\rho_1 = 0.4$ gives $\alpha = 0.428$ in Pullin and Grimshaw's notation. Based on their results, we had expected that overhanging depression waves were produced by our model, when the parameters were similar. Surprisingly, we find here that the wave solutions always become broad and flat with elevations consistent with the conjugate flow results (Fig. 13(a)), however. Broad and flat waves were also found for the two-layer fluid, where computations are performed with $\hat{h}_1/\hat{h}_3$ up to 100 (Fig. 13(b)). (In this case $N = 600$. Several intermediate amplitudes are calculated but not shown.) The difference between the overhanging extreme waves of elevation and the broad and flat waves of depression is noticeable. The latter result may indicate that very large waves of depression do not become overhanging. This is different from what can be indicated by the computations of Pullin and Grimshaw, where speed amplitude plot of depression waves had a limited maximal maximal amplitude (in the two-layer case) when $\hat{h}_1/\hat{h}_3 = \infty$ and their α was equal to 0.2. The latter corresponds to $\rho_3/\rho_1 = 2/3$, i.e. a smaller jump in the density than in the present computations.

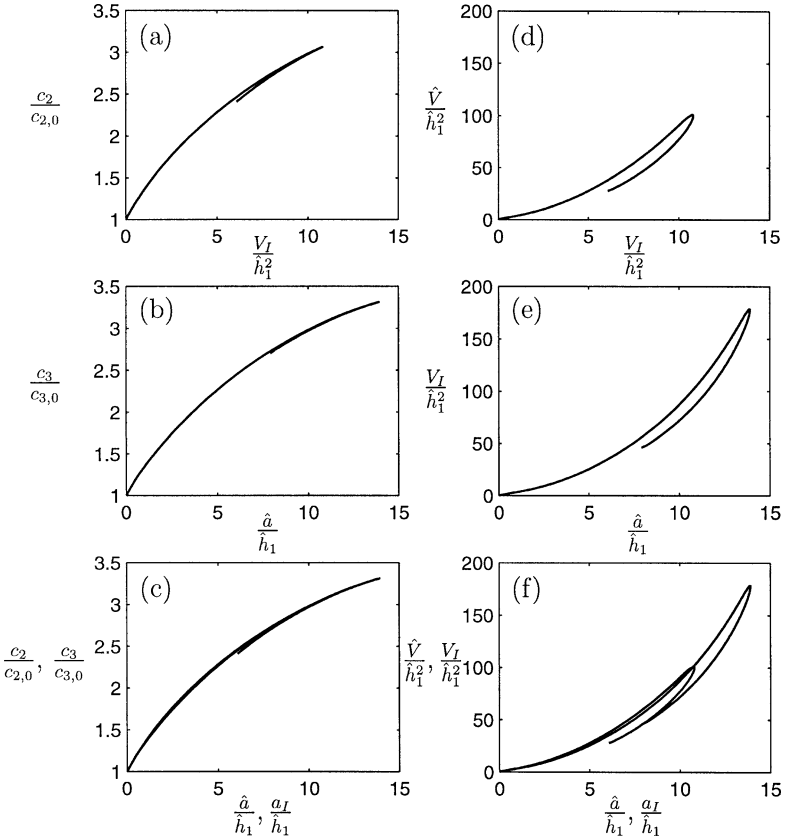

Fig. 12. The branch of solutions from wich the overhanging waves in Figs. 10, (b)–(c), and 11, (b)–(c), are taken. The propagation velocity is scaled by the linear velocity of the two-layer fluid (a), the linear velocity of the three-layer fluid (b). In (c) both (a) and (b) are visualized. The volume under I (d) for the two-layer fluid, under G (e) for the three-layer fluid and both (f). All results are plotted versus amplitude of I for the two-layer fluid and versus the amplitude of G for the three-layer fluid.

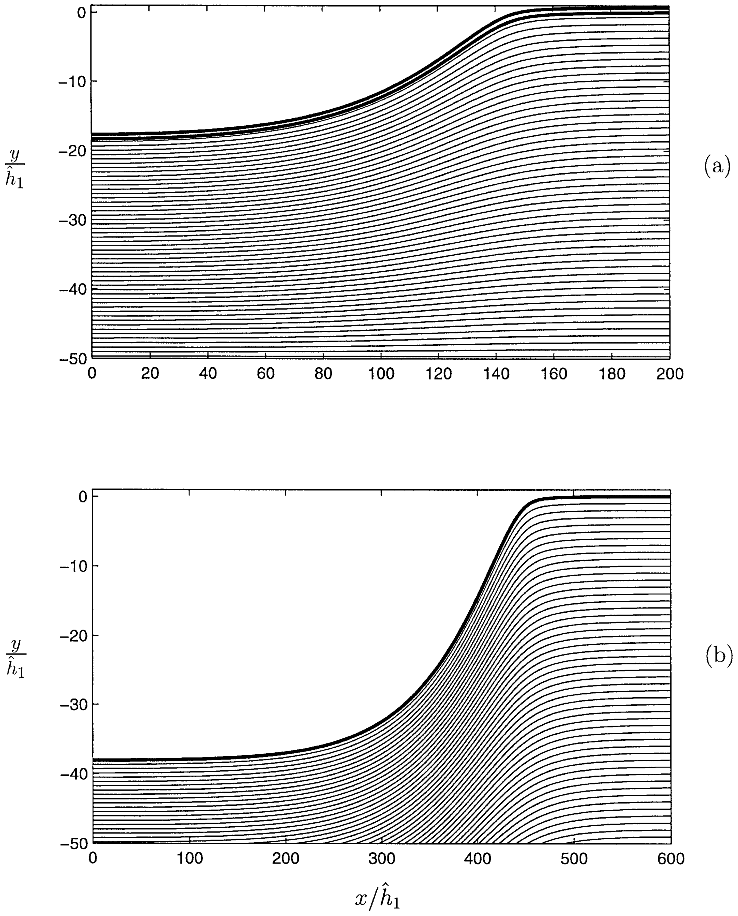

Fig. 13. Broad depression solitary waves with maximal amplitude. (a) Three-layer solution with $\hat{h}_1/\hat{h}_3 = 50$, $h_2 = h_3$, $\rho_3/\rho_1 = 0.4$, $\rho_2 = (\rho_1 + \rho_3)/2$, $N = 300$. Non-linear wave velocity is $c/c_0 = 3.361\ldots$. (b) Two-layer solution with $\hat{h}_1/\hat{h}_3 = 100$, $\rho_3/\rho_1 = 0.4$, $N = 600$. Non-linear wave velocity is $c/c_0 = 3.942\ldots$.

5. Conclusions

We have presented a fully nonlinear numerical method for calculation of symmetric solitary waves in a three-layer fluid. The method is based on a boundary integral formulation. The model is applied to compute steep and even overhanging waves. Both non-periodic and periodic versions of the scheme are derived. Simplified equations for three-layer conjugate flows are derived in parallel. Convergence of the full method is tested and results are obtained to graphical accuracy. The number of points on each interface is varied between 100 and 240, depending on the steepness of the wave. In a few of the computations $N = 600$ was used. We also extend existing relations in single- and two-layer flows between mass, momentum and kinetic energy to three-layer flows. Results of the full equations are compared with the conjugate flow solutions. Three-layer solutions are compared with corresponding two-layer solutions.

Mode-one and mode-two waves have been investigated. For mode-one waves the following results were obtained. In three-layer conjugate flows the middle line of the pycnocline attains a higher maximal elevation than in two-layer flows. The wave speed is smaller in the former than in the latter case, however. Detailed velocity-profiles due to the full equations were visualized for both three- and two-layer fluids, for moderate thickness ratio between the upper and lower layer ($\hat{h}_3/\hat{h}_1 = 4$). $\hat{h}_3$ and $\hat{h}_1$ are defined in Eq. (11), see also Fig. 1. Computations were also produced by the full method close to the Boussinesq limit for $\hat{h}_3/\hat{h}_1$ up to 50. The wave-amplitude was gradually increased until broad and flat-crested solitary waves were obtained. The waves satisfied the conjugate flow solutions. (Results were not shown.)

Computations of extreme mode-one waves were discussed in Section 4 for large thickness ratios and density ratios not close to unity. In the case when the upper layer is much larger than the two other layers ($\hat{h}_3/\hat{h}_1 \gg 1$, $h_2/h_1 = 1$) we generalize existing results for overhanging solitary waves in a two-layer fluid (Pullin and Grimshaw [8]) to the three-layer case. We find that the overhanging waves become more pronounced and the amplitude becomes larger in the three-layer than in the two-layer fluid. The results here confirm that the limiting configuration of solitary waves of elevation is overhanging waves, also in the three-layer case.

We have also investigated waves of depression when the lower layer is much larger than the two other layers ($\hat{h}_1/\hat{h}_3 \gg 1$, $h_2/h_1 = 1$, density ratios not close to unity). Large-amplitude solutions were in this case always broad and flat with excursions consistent with those of conjugate flows. This is true both for three- and two-layer fluid. (Computations for two-layer flows were performed for $\hat{h}_1/\hat{h}_3$ up to 100.) The difference between the overhanging extreme waves of elevation and the broad and flat waves of depression is noticeable. The latter result may indicate that very large waves of depression do not become overhanging. This is different from what was indicated by the computations of Pullin and Grimshaw [8]. We note that, e.g., Sha and Vanden-Broeck [26] confirm previous computations of overhanging solitary waves of elevation. Their computations of broad depression waves are always with moderate value of $\hat{h}_1/\hat{h}_3$.

On this point we mention that Laget and Dias [27], Section 5, summarizing the literature and performing a lot of computations on large interfacial gravity waves (for two-layer fluid), could not determine whether or not overhanging or broadening of the waves occurred as limiting configuration. This is in contrast to what we find here: in the Boussinesq limit the waves always become broad, and, for a large density jump, upward pointing waves always become overhanging, while downward pointing waves always become broad (one layer being much thicker than the other).

In the case of waves of mode-two, we first examined three-layer conjugate flows. In our numerical examples the thicknesses of the outer layers were put equal, while the thickness of the middle layer was varied. The densities were chosen close to the Boussinesq limit. The equations of conjugate flows produced either three or one large amplitude solutions, depending on the outer layer thicknesses, if they were larger or smaller, respectively, than a certain constant times the middle layer thickness. This was also found by Lamb [16] who investigated the Boussinesq limit analytically, in parallel to the present work. In addition to the solution(s) mentioned above, there is a very small mode-one solution, which vanishes in the Boussinesq limit, however.

Attempts were made to calculate solitary waves of mode-two using the full equations, but no satisfactory results were found. The explanation for this is obviously that a numerical solution of mode-two waves will also contain a train of short mode-one waves traveling with the same speed as the mode-two wave (Akylas and Grimshaw [18]; Boyd [21]; Michallet and Dias [19,20]). The short waves, that also are present in the far-field, are non-trivial to account for at the truncation of the computational domain. Preliminar computations were performed with a periodic version of the mathematical model. A series of waves of mode-two, with increasing amplitude, were obtained by gradually expanding the volume of the middle layer. Almost the largest mode-two wave we computed became close to one of the conjugate flow solutions. A train of mode-one waves was superimposed on the mode-two wave, with amplitude ranging from a small to a large value depending on the volume of the mode-two wave. In the most pronounced case the mode-one waves significantly affected the mode-two wave. The computations here, for mode-two waves, supplement those of Akylas and Grimshaw [18] and Michallet and Dias [19,20], investigating either quite different configurations or parameter-ranges.

Computational aspects of generalized mode-two waves are still unclear. This includes particularly the closure of the equations at the periodic boundaries and the effect of the imposed wave-length on the computations. On these points, more investigations are required.

Acknowledgements

Parts of the work of the first author was done while he was an employee at the Norwegian Defense Research Establishment and Østfold College. The support by the Strategic University Program "General Analysis of Realistic Ocean Waves" funded by the Research Council of Norway is gratefully acknowledged.

Appendix A. Discrete equations and computational algorithm

As done by Grue et al. [1], we parameterize the interfaces by introducing variables ξ and $\hat{\xi}$, which are continuous and monotonic along the interfaces, and let $z_I = \chi(\xi)$ describe the interface I and $z_J = \zeta(\hat{\xi})$ describe the interface J. We evaluate χ and ζ at integer values of ξ and $\hat{\xi}$. These points serve as collocation points of the discrete equations. For convenience, we will from now use the variable ξ for both ξ and $\hat{\xi}$.

Let $\gamma_{1I}(\xi) = \phi_{1Is}|\chi_\xi|$ be the scaled tangential velocity of the fluid in layer 1 on I. The complex velocity in layer 1 on I may then be expressed by $q_{1I}(\chi(\xi)) = \gamma_{1I}(\xi)/\chi_\xi(\xi)$. In general, we define γ_{kj} to be the scaled tangential velocity in layer k (1, 2, or 3), on interface j (I or J), such that the actual tangential velocities are $\gamma_{kI}/|\chi_\xi|$, $k = 1, 2$, and $\gamma_{kJ}/|\zeta_\xi|$, $k = 2, 3$, on interface I and J, respectively.

Introducing the scaled tangential velocities and multiplying by χ_ξ or ζ_ξ, the imaginary parts of (1)–(3) read, for z' on the interfaces,

$$\pi\,\mathrm{Re}\big(\gamma'_{1I} + c\chi'_\xi\big) = \mathrm{Im}\,\mathrm{PV}\int_I \left[\frac{\chi'_\xi}{\chi'-\chi} - \left(\frac{\chi'_\xi}{\chi'-\chi^*+2\mathrm{i}h_1}\right)^*\right](\gamma_{1I}+c\chi_\xi)\,\mathrm{d}\xi, \tag{23a}$$

$$-\pi\,\mathrm{Re}\big(\gamma'_{2I} + c\chi'_\xi\big) = \mathrm{Im}\,\mathrm{PV}\int_I \frac{\chi'_\xi}{\chi'-\chi}(\gamma_{2I}+c\chi_\xi)\,\mathrm{d}\xi - \mathrm{Im}\int_J \frac{\chi'_\xi}{\chi'-\zeta}(\gamma_{2J}+c\zeta_\xi)\,\mathrm{d}\xi, \tag{23b}$$

$$-\pi\,\mathrm{Re}\big(\gamma'_{2J} + c\zeta'_\xi\big) = \mathrm{Im}\int_I \frac{\zeta'_\xi}{\zeta'-\chi}(\gamma_{2I}+c\chi_\xi)\,\mathrm{d}\xi - \mathrm{Im}\,\mathrm{PV}\int_J \frac{\zeta'_\xi}{\zeta'-\zeta}(\gamma_{2J}+c\zeta_\xi)\,\mathrm{d}\xi, \tag{23c}$$

$$-\pi\,\mathrm{Re}\big(\gamma'_{3J} + c\zeta'_\xi\big) = \mathrm{Im}\,\mathrm{PV}\int_J \left[\frac{\zeta'_\xi}{\zeta'-\zeta} - \left(\frac{\zeta'_\xi}{\zeta'-\zeta^*-2\mathrm{i}(h_2+h_3)}\right)^*\right](\gamma_{3J}+c\zeta_\xi)\,\mathrm{d}\xi, \tag{23d}$$

where $(\,)'$ means that the value is taken at $\xi = \xi'$.

We will only consider solutions symmetric with respect to $x = 0$. Symmetry of the interfaces and all other streamlines, gives the following relation for the velocities: $q_k(-z^*) = q_k(z)^*$ for $k = 1, 2, 3$. Utilizing the symmetry, we rewrite (23a)–(23d) and obtain:

$$\begin{aligned}\pi\,\mathrm{Re}\big(\gamma'_{1I} + c\chi'_\xi\big) ={}& \mathrm{Im}\,\mathrm{PV}\int_{I_+} \left[\frac{\chi'_\xi}{\chi'-\chi} - \left(\frac{\chi'_\xi}{\chi'+\chi^*}\right)^*\right](\gamma_{1I}+c\chi_\xi)\,\mathrm{d}\xi\\ &- \mathrm{Im}\int_{I_+} \left[\left(\frac{\chi'_\xi}{\chi'-\chi^*+2\mathrm{i}h_1}\right)^* - \frac{\chi'_\xi}{\chi'+\chi+2\mathrm{i}h_1}\right](\gamma_{1I}+c\chi_\xi)\,\mathrm{d}\xi,\end{aligned} \tag{24a}$$

$$\begin{aligned}-\pi\,\mathrm{Re}\big(\gamma'_{2I} + c\chi'_\xi\big) ={}& \mathrm{Im}\,\mathrm{PV}\int_{I_+} \left[\frac{\chi'_\xi}{\chi'-\chi} - \left(\frac{\chi'_\xi}{\chi'+\chi^*}\right)^*\right](\gamma_{2I}+c\chi_\xi)\,\mathrm{d}\xi\\ &- \mathrm{Im}\int_{J_+} \left[\frac{\chi'_\xi}{\chi'-\zeta} - \left(\frac{\chi'_\xi}{\chi'+\zeta^*}\right)^*\right](\gamma_{2J}+c\zeta_\xi)\,\mathrm{d}\xi,\end{aligned} \tag{24b}$$

$$\begin{aligned}-\pi\,\mathrm{Re}\big(\gamma'_{2J} + c\zeta'_\xi\big) ={}& \mathrm{Im}\int_{I_+} \left[\frac{\zeta'_\xi}{\zeta'-\chi} - \left(\frac{\zeta'_\xi}{\zeta'+\chi^*}\right)^*\right](\gamma_{2I}+c\chi_\xi)\,\mathrm{d}\xi\\ &- \mathrm{Im}\,\mathrm{PV}\int_{J_+} \left[\frac{\zeta'_\xi}{\zeta'-\zeta} - \left(\frac{\zeta'_\xi}{\zeta'+\zeta^*}\right)^*\right](\gamma_{2J}+c\zeta_\xi)\,\mathrm{d}\xi,\end{aligned} \tag{24c}$$

$$\begin{aligned}-\pi\,\mathrm{Re}\big(\gamma'_{3J} + c\zeta'_\xi\big) ={}& \mathrm{Im}\,\mathrm{PV}\int_{J_+} \left[\frac{\zeta'_\xi}{\zeta'-\zeta} - \left(\frac{\zeta'_\xi}{\zeta'+\zeta^*}\right)^*\right](\gamma_{3J}+c\zeta_\xi)\,\mathrm{d}\xi\\ &- \mathrm{Im}\int_{J_+} \left[\left(\frac{\zeta'_\xi}{\zeta'-\zeta^*-2\mathrm{i}(h_2+h_3)}\right)^* - \frac{\zeta'_\xi}{\zeta'+\zeta-2\mathrm{i}(h_2+h_3)}\right](\gamma_{3J}+c\zeta_\xi)\,\mathrm{d}\xi,\end{aligned} \tag{24d}$$

where I_+ and J_+ are the parts of I and J, respectively, with $0 \leqslant x \leqslant \infty$.

We let $\xi = 1$ be at the collocation points at the symmetry plane $x = 0$, and distribute N_I and N_J points on I_+ and J_+, respectively. The integrals in (24a)–(24d) are evaluated using the trapezoid rule, except in the vicinity of the poles, where we adopt the procedure described by Dold and Peregrine [28]. In the interval $[\xi' - 1/2, \xi' + 1/2]$ around a pole, the integrand is expanded in powers of $(\xi - \xi')$. The principal value integral of a smooth function f is then approximated by the following scheme:

$$\begin{aligned}\mathrm{PV}\int\limits_{I_+}\frac{\chi'_\xi}{\chi'-\chi(\xi)}f(\xi)\,\mathrm{d}\xi &= \mathrm{PV}\int\limits_{\xi'-1/2}^{\xi'+1/2}\frac{\chi'_\xi}{\chi'-\chi}f(\xi)\,\mathrm{d}\xi+\frac{1}{2}\frac{\chi'_\xi}{\chi'-\chi(1)}f(1)+\sum_{\xi=2,\,\xi\neq\xi'}^{N_I}\frac{\chi'_\xi}{\chi'-\chi}f(\xi)\\ &= \frac{\chi'_{\xi\xi}}{2\chi'_\xi}f'-f'_\xi+\frac{1}{2}\frac{\chi'_\xi}{\chi'-\chi(1)}f(1)+\sum_{\xi=2,\,\xi\neq\xi'}^{N_I}\frac{\chi'_\xi}{\chi'-\chi}f(\xi).\end{aligned}\tag{25}$$

Here, we have assumed that $\xi'\neq 1$. In the case of $\xi'=1$, a similar expression is easily found.

The discretized versions of Eqs. (24a)–(24d) now read:

$$\pi\,\mathrm{Re}\big(\gamma'_{1I}+c\chi'_\xi\big)=\mathrm{Im}\sum_{\xi=1}^{N_I}\big[M_{II}(\xi',\xi)-M_{1II}(\xi',\xi)\big](\gamma_{1I}+c\chi_\xi)-c\,\mathrm{Im}\big(\chi'_{\xi\xi}\big),\tag{26a}$$

$$-\pi\,\mathrm{Re}\big(\gamma'_{2I}+c\chi'_\xi\big)=\mathrm{Im}\sum_{\xi=1}^{N_I}M_{II}(\xi',\xi)(\gamma_{2I}+c\chi_\xi)-c\,\mathrm{Im}\big(\chi'_{\xi\xi}\big)-\mathrm{Im}\sum_{\xi=1}^{N_J}M_{IJ}(\xi',\xi)(\gamma_{2J}+c\zeta_\xi),\tag{26b}$$

$$-\pi\,\mathrm{Re}\big(\gamma'_{2J}+c\zeta'_\xi\big)=\mathrm{Im}\sum_{\xi=1}^{N_I}M_{JI}(\xi',\xi)(\gamma_{2I}+c\chi_\xi)-\mathrm{Im}\sum_{\xi=1}^{N_J}M_{JJ}(\xi',\xi)(\gamma_{2J}+c\zeta_\xi)+c\,\mathrm{Im}\big(\zeta'_{\xi\xi}\big),\tag{26c}$$

$$\pi\,\mathrm{Re}\big(\gamma'_{3J}+c\zeta'_\xi\big)=\mathrm{Im}\sum_{\xi=1}^{N_J}\big[M_{JJ}(\xi',\xi)-M_{3JJ}(\xi',\xi)\big](\gamma_{3J}+c\zeta_\xi)-c\,\mathrm{Im}\big(\zeta'_{\xi\xi}\big),\tag{26d}$$

where

$$\mathcal{M}_{II}(\xi',\xi)=\begin{cases}\chi'_\xi/(\chi'-\chi)-\big(\chi'_\xi/(\chi'+\chi^*)\big)^*, & \xi>1,\xi'\neq\xi,\\ \frac{1}{2}\big[\chi'_\xi/(\chi'-\chi)-\big(\chi'_\xi/(\chi'+\chi^*)\big)^*\big], & \xi=1,\xi'>1,\\ \chi_{\xi\xi}/(2\chi_\xi)-\big(\chi'_\xi/(\chi'+\chi^*)\big)^*, & \xi>1,\xi'=\xi,\\ \chi_{\xi\xi}/(2\chi_\xi), & \xi=\xi'=1,\end{cases}\tag{27a}$$

$$\mathcal{M}_{1II}(\xi',\xi)=\begin{cases}\big(\chi'_\xi/(\chi'-\chi^*+2\mathrm{i}h_1)\big)^*-\chi'_\xi/(\chi'+\chi+2\mathrm{i}h_1), & \xi>1,\\ \frac{1}{2}\big[\big(\chi'_\xi/(\chi'-\chi^*+2\mathrm{i}h_1)\big)^*-\chi'_\xi/(\chi'+\chi+2\mathrm{i}h_1)\big], & \xi=1,\end{cases}\tag{27b}$$

$$\mathcal{M}_{IJ}(\xi',\xi)=\begin{cases}\chi'_\xi/(\chi'-\zeta)-\big(\chi'_\xi/(\chi'+\zeta^*)\big)^*, & \xi>1,\\ \frac{1}{2}\big[\chi'_\xi/(\chi'-\zeta)-\big(\chi'_\xi/(\chi'+\zeta^*)\big)^*\big], & \xi=1,\end{cases}\tag{27c}$$

$$\mathcal{M}_{JI}(\xi',\xi)=\begin{cases}\zeta'_\xi/(\zeta'-\chi)-\big(\zeta'_\xi/(\zeta'+\chi^*)\big)^*, & \xi>1,\\ \frac{1}{2}\big[\zeta'_\xi/(\zeta'-\chi)-\big(\zeta'_\xi/(\zeta'+\chi^*)\big)^*\big], & \xi=1,\end{cases}\tag{27d}$$

$$\mathcal{M}_{JJ}(\xi',\xi)=\begin{cases}\zeta'_\xi/(\zeta'-\zeta)-\big(\zeta'_\xi/(\zeta'+\zeta^*)\big)^*, & \xi>1,\xi'\neq\xi,\\ \frac{1}{2}\big[\zeta'_\xi/(\zeta'-\zeta)-\big(\zeta'_\xi/(\zeta'+\zeta^*)\big)^*\big], & \xi=1,\xi'>1,\\ \zeta_{\xi\xi}/(2\zeta_\xi)-\big(\zeta'_\xi/(\zeta'+\zeta^*)\big)^*, & \xi>1,\xi'=\xi,\\ \zeta_{\xi\xi}/(2\zeta_\xi), & \xi=\xi'=1,\end{cases}\tag{27e}$$

$$\mathcal{M}_{3JJ}(\xi',\xi)=\begin{cases}\big(\zeta'_\xi\big/\big(\zeta'-\zeta^*-2\mathrm{i}\hat{h}\big)\big)^*-\zeta'_\xi\big/\big(\zeta'+\zeta-2\mathrm{i}\hat{h}\big), & \xi>1,\\ \frac{1}{2}\big[\big(\zeta'_\xi\big/\big(\zeta'-\zeta^*-2\mathrm{i}\hat{h}\big)\big)^*-\zeta'_\xi\big/\big(\zeta'+\zeta-2\mathrm{i}\hat{h}\big)\big], & \xi=1.\end{cases}\tag{27f}$$

We now rewrite the dynamic boundary conditions in Eqs. (4a)–(4b) in terms of the scaled tangential derivatives:

$$\frac{1}{2}\rho_1\bigg(c^2-\frac{{\gamma_{1I}}^2}{|\chi_\xi|^2}\bigg)-\frac{1}{2}\rho_2\bigg(c^2-\frac{{\gamma_{2I}}^2}{|\chi_\xi|^2}\bigg)-(\rho_1-\rho_2)g\,\mathrm{Im}(\chi)=0,\tag{28a}$$

$$\frac{1}{2}\rho_2\bigg(c^2-\frac{{\gamma_{2J}}^2}{|\zeta_\xi|^2}\bigg)-\frac{1}{2}\rho_3\bigg(c^2-\frac{{\gamma_{3J}}^2}{|\zeta_\xi|^2}\bigg)-(\rho_2-\rho_3)g\big(\mathrm{Im}(\zeta)-h_2\big)=0.\tag{28b}$$

These conditions are applied on each collocation point, e.g., at integer values of ξ.

The described mathematical model is an integrodifferential method, since both integrals and derivatives of the unknown quantities are involved in the equations. The numerical scheme then includes both sums and finite differences. As done by Grue et al. [11], differentiations with respect to ξ of first and second order are approximated by applying the four and five point Lagrangian differentiation formula for first and second derivatives, respectively. Applied on a function $f(\xi)$, these finite difference formulas become

$$f_\xi(\xi) = \frac{1}{12}\big(-f(\xi+2) + 8f(\xi+1) - 8f(\xi-1) + f(\xi-2)\big), \tag{29}$$

$$f_{\xi\xi}(\xi) = \frac{1}{12}\big(-f(\xi+2) + 16f(\xi+1) - 30f(\xi) + 16f(\xi-1) - f(\xi-2)\big). \tag{30}$$

So far, the only requirement imposed on the distribution of the collocation points is that the first one, with $\xi = 1$, should be at the symmetry plane $x = 0$. This applies for both I_+ and J_+. By Grue et al. [11], all the collocation points were fixed with equal intervals in the x-coordinate. This simple requirement was chosen because no extremely steep or overhanging waves were considered. To allow for such waves as well, we distribute the points such that the distance along a straight line between adjacent points are equal. In addition, the x-values of the truncated ends are set to fixed values. We define the distances between the collocation points, $\Delta L_I(\xi)$ and $\Delta L_J(\xi)$, as

$$\Delta L_I(\xi) = \big|\chi(\xi) - \chi(\xi-1)\big|, \quad \xi = 2, 3, \ldots, N_I, \tag{31a}$$

$$\Delta L_J(\xi) = \big|\zeta(\xi) - \zeta(\xi-1)\big|, \quad \xi = 2, 3, \ldots, N_J. \tag{31b}$$

The equations describing the collocation point distribution are now for interface I_+:

$$\mathrm{Re}\big(\chi(1)\big) = 0, \tag{32a}$$

$$\Delta L_I(\xi) - \Delta L_I(\xi-1) = 0, \quad \xi = 3, \ldots, N_I, \tag{32b}$$

$$\mathrm{Re}\big(\chi(N_I)\big) = L, \tag{32c}$$

and for interface J_+:

$$\mathrm{Re}\big(\zeta(1)\big) = 0, \tag{33a}$$

$$\Delta L_J(\xi) - \Delta L_J(\xi-1) = 0, \quad \xi = 3, \ldots, N_J, \tag{33b}$$

$$\mathrm{Re}\big(\zeta(N_J)\big) = L, \tag{33c}$$

where L is a given length of the truncated I_+ and J_+ along the x-axis.

We want the tail of I_+ to approach the x-axis. This means that $\mathrm{Im}(\chi(N_I)) = 0$. Similarly, we let $\mathrm{Im}(\zeta(N_J)) = h_2$. From numerical experiments we also find that it is advantageous to control the behavior of the truncated ends of the interfaces by requiring $\mathrm{Im}(\chi_{\xi\xi}(N_I)) = 0$ and $\mathrm{Im}(\zeta_{\xi\xi}(N_J)) = 0$. In addition, when applying the Laplacian difference formulas near and at the truncated ends, we assume a symmetric extrapolation of the interfaces, such that $\mathrm{Im}(\chi_\xi(N_I))$ and $\mathrm{Im}(\zeta_\xi(N_J))$ implicitly are zero. The four explicit conditions mentioned, applied at the truncated ends of I_+ and J_+, replace the integral equations (26a)–(26d) at the end points. The integral equations are then evaluated at $\xi' = 1, \ldots, N_I - 1$ or $\xi' = 1, \ldots, N_J - 1$.

The unknown variables are $\chi(\xi)$, $\gamma_{1I}(\xi)$, $\gamma_{2I}(\xi)$, $\zeta(\xi)$, $\gamma_{2J}(\xi)$, $\gamma_{3J}(\xi)$ and c. This gives a total of $4N_I + 4N_J + 1$ real variables, since both the real and imaginary parts of $\chi(\xi)$ and $\zeta(\xi)$ are unknown. The total number of equations given so far is, however, only $4N_I + 4N_J$. The last missing equation is the one characterizing the solution we seek. This may be an equation giving the amplitude of either the wave profile on I or J, the propagation speed, the volume under an interface, or any other physical quantity characterizing the solution.

The results presented in this paper, are calculated with different choices of the last characterizing equation. For example, when calculating conjugate flow solutions, the amplitude reaches an upper bound, but by requiring increasingly larger volumes under the interface, broader solutions are found.

The nonlinear system of equations is solved by applying Newton–Raphson's method, with a first-order finite difference approximation of the Jacobian matrix. This finite difference approximation is simple to implement. Alternatively, it is possible to deduce the exact expression of the Jacobian matrix from the discretized equations, but differentiating the integral equations (26a)–(26d) becomes rather involved. This procedure is avoided.

When straightforward finite differencing is applied to obtain the elements of the Jacobian matrix corresponding to one of the integral equations in (26a)–(26d), a summation over N_I or N_J (or both) number of elements must be performed. The number of operations required to calculate the complete Jacobian matrix is proportional to N^3, where N denotes the total number of unknowns. The constant of proportionality is also quite large. Thus it is important to reduce the number of operations of the numerical scheme. This is achieved by first utilizing the fact that some blocks of the Jacobian matrix are zero. Next, we exploit the fact that most of the terms of the sums in Eqs. (26a)–(26d) are constant when a quantity at a single collocation point is varied only. For every element of the Jacobian matrix, we then only recalculate the part of a summation that is affected by a change of the appropriate unknown. The number of operations needed to calculate a single element of the Jacobian matrix is then fixed, and is not increasing with N. The total number of operations needed to calculate the Jacobian matrix is now proportional to N^2. This is of the same order as if the matrix had been calculated by analytical differentiation of the discrete equations.

Numerical experiments show that a good initial guess of the propagation speed is important for convergence of the scheme. The long wave speed derived in Section 3.2 is used as the initial guess. This speed also serves as a reference for the nonlinear solutions. The initial shapes of the interfaces seem to be of minor importance.

The numerical scheme was implemented in Matlab. The extensive summations in Eqs. (26) and (27) are easily formulated as matrix multiplications in order to utilize the matrix features of Matlab.

Appendix B. Conjugate flow equations in the Boussinesq limit

Figure 2 shows that c and $\hat{c}$ become equal and that the normalized differences $a_I - \hat{a}$ and $a_I - h_2 - \hat{a}$ become linear functions of $h_2/(2\hat{h}_1)$ when the relative thickness of the upper layer becomes large ($h_1/h_3 \ll 1, h_2/h_3 \ll 1$). These results may be obtained from the conjugate flows equations in the Boussinesq limit. We proceed as follows: substituting (5) into (9a)–(10) we obtain, after some manipulations:

$$c^2\left[\frac{h_2^2}{(a_J - a_I)^2} - \frac{h_1^2}{(h_1 + a_I)^2}\right] = g' a_I, \tag{34}$$

$$c^2\left[\frac{h_3^2}{(h_3 - (a_J - h_2))^2} - \frac{h_1^2}{(h_1 + a_I)^2}\right] = g'(a_I + a_J - h_2), \tag{35}$$

$$c^2\left[\frac{h_1^3}{(h_1 + a_I)^2} + \frac{h_2^3}{(a_J - a_I)^2} + \frac{h_3^3}{(h_3 - (a_J - h_2))^2} - H\right] = \frac{3}{2}g'\bigl(a_I^2 + (a_J - h_2)^2\bigr). \tag{36}$$

We then introduce $a = a_I/h_3$, $b = (a_J - h_2)/h_3$, $A = a + b$, $B = a - b$, and divide (34) by (35) and (36) by (35), giving

$$(1 - b)^2 \frac{(h_2/h_3)^2}{(B - h_2/h_3)^2}\bigl[1 + \mathrm{O}\bigl((h_1/h_3)^2\bigr)\bigr] = \frac{a}{A}, \tag{37}$$

$$(1 - b)^2\left[\frac{1}{(1 - b)^2} - 1 + \frac{(h_2/h_3)^3}{(B - h_2/h_3)^2} - \frac{h_1 + h_2}{h_3}\right]\bigl[1 + \mathrm{O}\bigl((h_1/h_3)^3\bigr)\bigr] = \frac{3}{4}\bigl(A + B^2/A\bigr). \tag{38}$$

Expanding $A = A_0 + A_1$, where $A = A_0$ for $h_1/h_3 = 0$ and $h_2/h_3 = 0$, using that $b = (A - B)/2$ and $a = (A + B)/2$, (38) gives that $A_0 = 1$. Eqs. (38) and (38) then give

$$B = \left(-\frac{\sqrt{2}}{2} + 1\right)\frac{h_2}{h_3}, \qquad A_1 = -2B + \frac{h_2 - h_1}{h_3}, \tag{39}$$

and it follows that

$$\frac{a_I - \hat{a}}{\hat{h}_1} = \frac{\sqrt{2}}{2}\frac{h_2}{2\hat{h}_1}, \qquad \frac{a_J - h_2 - \hat{a}}{\hat{h}_1} = \left(\frac{3\sqrt{2}}{2} - 2\right)\frac{h_2}{2\hat{h}_1}, \tag{40}$$

which are valid in the Boussinesq limit when $h_1/h_3 \ll 1$, $h_2/h_3 \ll 1$. In (40), $\hat{a} = (\hat{h}_3 - \hat{h}_1)/2$. It also follows from the equations that $c = \hat{c}$ in the Boussinesq limit when $h_1/h_3 \ll 1$, $h_2/h_3 \ll 1$. The results in (40) confirm the numerical predictions in Fig. 2 with $\rho_3/\rho_1 = 0.9775$.

Appendix C. Integral properties

It is well known that exact relations between integral properties of both surface and internal solitary waves exist. Longuet-Higgins [29] discussed five relations for surface waves. We will in this chapter consider such relationships between momentum, kinetic energy and mass of the solitary wave. Such relations were originally proved by McCowan [30] for surface waves. Pullin and Grimshaw [8] showed that the relations are easily extended to interfacial waves in a two-layer fluid bounded by rigid lids on top and bottom. Pennel [31] extended the relations further to include also solitary waves in a two-layer fluid with a free surface on top. Such relations were also later discussed by Evans and Ford [32]. Previous results are here generalized to the case of a three-layer fluid. The derived relations serve as checks in the numerical computations.

We define M_k as the difference in mass of layer k, due to the solitary wave, compared to the undisturbed fluid. For each layer we obtain

$$M_1 = \rho_1 \int_I y x_s \,\mathrm{d}s, \tag{41a}$$

$$M_2 = \rho_2 \int_J (y - h_2) x_s \,\mathrm{d}s - \rho_2 \int_I y x_s \,\mathrm{d}s, \tag{41b}$$

$$M_3 = -\rho_3 \int_J (y - h_2) x_s \,\mathrm{d}s. \tag{41c}$$

The momentum in the positive x-direction in each layer is

$$P_k = \rho_k \int_{\Omega_k} \tilde{u}\,\mathrm{d}\Omega, \quad k = 1, 2, 3, \tag{42}$$

where Ω_k is the domain of fluid k and a tilde indicates reference to the laboratory frame (in contrast to the frame of reference moving with the wave). The circulation along an open curve of layer k is

$$C_k = \tilde{\phi}_k \big|_{x\to-\infty}^{x\to\infty}. \tag{43}$$

To derive a relation between P_k and M_k, we follow essentially the same procedure as Longuet-Higgins [29] for free surface waves. A slight reformulation here means that the proof is valid also for overhanging interfaces. First we note that conservation of mass yields

$$\int_{\text{layer}\,k} u\,\mathrm{d}y = -h_k c, \tag{44}$$

where we may integrate over any cross section of layer k. For values of x for which the bounding wave profile is overhanging, the cross section of a layer consist of two separate regions. However, conservation of mass still yields Eq. (44).

The momentum of layer k, defined in Eq. (42), may now be expressed as

$$P_k = \rho_k \int_{-\infty}^{\infty} \int_{\text{layer}\,k} (u + c)\,\mathrm{d}y\,\mathrm{d}x = c M_k. \tag{45}$$

McCowan [30] proved a simple relationship between the kinetic energy, momentum and circulation of a solitary surface wave, which read $\widetilde{T} = (1/2)c(P - \rho h C)$. Here $\widetilde{T}$, P and ρ are the kinetic energy, momentum and density, respectively, of the single fluid layer. The circulation, C, is defined similarly to Eq. (43). Longuet-Higgins [33] presented a simple proof of this relation. Pullin and Grimshaw [8] found a similar expression for solitary waves in a two-layer fluid bounded by rigid lids on the top and bottom. The layers were of constant density and vorticity. Pennel [31] extended the relation to solitary waves on a two-layer fluid with a free surface on top (and zero vorticity in each layer). We extend his results and obtain the kinetic energy for solitary waves on a three-layer fluid:

$$\widetilde{T} = \widetilde{T}_1 + \widetilde{T}_2 + \widetilde{T}_3, \tag{46}$$

where

$$\widetilde{T}_k = \frac{1}{2} c (P_k - \rho_k h_k C_k), \quad k = 1, 2, 3. \tag{47}$$

To prove this relation, we follow Longuet-Higgins [33] for each of the layers, only with slight differences such that the proof is valid also for overhanging waves. First consider the fluid of layer k between two distant limits $x = \pm X$. Let ω_k denote the fluid domain of layer k between these limits. The stream function, ψ_k, is constant on the lower and upper boundaries of ω_k. At the vertical cross sections at the distant limits $x = \pm X$, the flow is uniform such that ϕ_k is independent of the vertical coordinate. Utilizing this by integrating the squared velocity in the frame of reference moving with the wave, we obtain

$$\iint_{\omega_k} \big(u^2 + v^2\big)\,\mathrm{d}x\,\mathrm{d}y = \iint_{\omega_k} \nabla \cdot (\psi \nabla \psi)\,\mathrm{d}x\,\mathrm{d}y = -\oint_{\partial\omega_k} \psi \frac{\partial \phi}{\partial s}\,\mathrm{d}s = \iint_{\omega_k} \mathrm{d}\psi\,\mathrm{d}\phi. \tag{48}$$

The kinetic energy, $\widetilde{T}_k$, of the fluid within ω_k is now determined by

$$\begin{aligned}\widetilde{T}_k \frac{2}{\rho_k} &= \iint\limits_{\omega_k} \left((u+c)^2 + v^2\right) \mathrm{d}x\, \mathrm{d}y = \iint\limits_{\omega_k} \mathrm{d}\psi\, \mathrm{d}\phi + c^2 \iint\limits_{\omega_k} \mathrm{d}x\, \mathrm{d}y + 2c \iint\limits_{\omega_k} u\, \mathrm{d}x\, \mathrm{d}y \\ &= -ch_k \phi_k|_{-X}^{X} + c^2 \iint\limits_{\omega_k} \mathrm{d}x\, \mathrm{d}y - 4c^2 h_k X = -ch_k \tilde{\phi}_k|_{-X}^{X} + c^2 \iint\limits_{\omega_k} \mathrm{d}x\, \mathrm{d}y - 2c^2 h_k X. \qquad (49)\end{aligned}$$

Here we have utilized that the difference in ψ_k between the upper and lower boundary is $-ch_k$, which is the constant volume flux of the layer. We have

$$\lim_{X\to\infty} \left(c^2 \iint\limits_{\omega_k} \mathrm{d}x\, \mathrm{d}y - 2c^2 h_k X \right) = c^2 M_k, \qquad (50)$$

and by using Eqs. (43) and (45) we obtain

$$\widetilde{T}_k = \frac{1}{2} c(cM_k - \rho_k h_k C_k) = \frac{1}{2} c(P_k - \rho_k h_k C_k). \qquad (51)$$

References

[1] J. Grue, H.A. Friis, E. Palm, P.-O. Rusås, A method for computing fully nonlinear interfacial waves, J. Fluid Mech. 351 (1997) 223.
[2] T. Duda., D.M. Farmer (Eds.), IOS/WHOI/ONR Internal Solitary Wave Workshop, Victoria B.C., Canada, Woods Hole Oceanographic Institution, Tech. Report WHOI-99-07, 1998.
[3] K.-K. Tung, T.F. Chan, T. Kubota, Large amplitude internal waves of permanent form, Stud. Appl. Math. 66 (1982) 1.
[4] B. Turkington, A. Eydeland, S. Wang, A computational method for solitary internal waves in a continuously stratified fluid, Stud. Appl. Math. 85 (1991) 93.
[5] K.G. Lamb, Numerical simulations of stratified inciscid flow over a smooth obstacle, J. Fluid Mech. 260 (1994) 1.
[6] J. Grue, A. Jensen, P.-O. Rusås, J.K. Sveen, Breaking and broadening of internal solitary waves, J. Fluid Mech. 414 (2000) 181.
[7] C.J. Amick, R.E.L. Turner, A global theory of internal solitary waves in two-fluid systems, Trans. Amer. Math. Soc. 298 (1986) 431.
[8] D.I. Pullin, R.H.J. Grimshaw, Finite amplitude solitary waves at the interface between two homogeneous fluids, Phys. Fluids 31 (1988) 3550.
[9] R.E.L. Turner, J.M. Vanden-Broeck, The limiting configuration of interfacial gravity waves, Phys. Fluids 29 (1986) 372.
[10] R.E.L. Turner, J.M. Vanden-Broeck, Broadening of interfacial solitary waves, Phys. Fluids 31 (1988) 2486.
[11] J. Grue, A. Jensen, P.-O. Rusås, J.K. Sveen, Properties of large amplitude internal waves, J. Fluid Mech. 380 (1999) 257.
[12] O.M. Phillips, The Dynamics of the Upper Ocean, Cambridge University Press, 1980.
[13] T.B. Benjamin, Internal waves of finite amplitude and permanent form, J. Fluid Mech. 25 (1966) 241.
[14] S.C. Mehrotra, R.E. Kelly, On the question of nonuniqueness of internal hydraulic jumps and drops in a two-fluid system, Tellus 25 (1973) 560.
[15] T. Kakutani, N. Yamasaki, Solitary waves on a two-layer fluid, J. Phys. Soc. Jap. 45 (1978) 674.
[16] K.G. Lamb, Conjugate flows for a three-layer fluid, Phys. Fluids 12 (2000) 2169.
[17] R.E. Davis, A. Acrivos, Solitary internal waves in deep water, J. Fluid Mech. 29 (1967) 593.
[18] T.R. Akylas, R. Grimshaw, Solitary internal waves with oscillatory tails, J. Fluid Mech. 242 (1992) 279.
[19] H. Michallet, F. Dias, Numerical study of generalized interfacial solitary waves, Phys. Fluids 11 (1999) 1502.
[20] H. Michallet, F. Dias, Non-linear resonance between short and long waves, in: Proc. 9th Int. Offshore and Polar Conf., Brest III, 1999, p. 193.
[21] J.P. Boyd, Weakly non-local solitary waves, in: Nohoul J.C.J., Jamart B.M. (Eds.), Mesoscale/Synoptic Coherent Structures in Geophysical Turbulence, Elsevier, 1989, pp. 103–112.
[22] P.M. Baines, Topographic Effects in Stratified Flows, Cambridge Monographs on Mechanics, Cambridge University Press, 1995.
[23] J.N. Moni, A.C. King, Guided and unguided interfacial solitary waves, Q. J. Mech. Appl. Math. 48 (1995) 21.
[24] P.O. Rusås, On nonlinear internal waves in two- and three-layer fluids, DSc thesis, Department of Mathematics, University of Oslo, 2000.
[25] D.I. Meiron, P.G. Saffman, Overhanging interfacial gracity waves of large amplitude, J. Fluid Mech. 129 (1983) 213.
[26] H. Sha, J.-M. Vanden-Broeck, Two-layer flows past a semicircular obstruction, Phys. Fluids A 5 (1993) 2661.
[27] O. Laget, F. Dias, Numerical computation of capillary-gravity interfacial solitary waves, J. Fluid Mech. 349 (1997) 221.
[28] J.W. Dold, D.H. Peregrine, An efficient boundary-integral equation method for steep unsteady water waves, in: K.W. Morton, M.J. Baines (Eds.), Numerical Methods for Fluid Dynamics, Vol. 2, Clarendon, 1985, p. 671.
[29] M.S. Longuet-Higgins, On the mass, momentum, energy and circulation of a solitary wave, Proc. Roy. Soc. London A Mat. 337 (1974) 1.
[30] J. McCowan, On the solitary wave, Philos. Mag. 32 (1891) 45.
[31] S. Pennel, A note on exact relations for solitary waves, Phys. Fluids A 2 (1990) 281.
[32] W.A.B. Evans, M.J. Ford, An integral equation approach to internal (2-layer) solitary waves, Phys. Fluids 8 (1996) 2032.
[33] M.S. Longuet-Higgins, J.D. Fenton, On the mass, momentum, energy and circulation of a solitary wave II, Proc. Roy. Soc. London A 340 (1974) 471.